

RESIDUAL STRESS MEASUREMENT USING X-RAY DIFFRACTION

A Thesis

by

OSMAN ANDEROGLU

Submitted to the Office of Graduate Studies of
Texas A&M University
in partial fulfillment of the requirements for the degree of

MASTER OF SCIENCE

December 2004

Major Subject: Mechanical Engineering

**RESIDUAL STRESS MEASUREMENT USING X-RAY
DIFFRACTION**

A Thesis

by

OSMAN ANDEROGLU

Submitted to the Office of Graduate Studies of
Texas A&M University
in partial fulfillment of the requirements for the degree of

MASTER OF SCIENCE

Approved as to style and content by:

Mustafa Yavuz
(Co-Chair of Committee)

Peter McIntyre
(Co-Chair of Committee)

Ibrahim Karaman
(Member)

Dennis L. O'Neal
(Head of Department)

December 2004

Major Subject: Mechanical Engineering

ABSTRACT

Residual Stress Measurement Using X-ray Diffraction.

(December 2004)

Osman Anderoglu, B.S., Bogazici University, Turkey

Chair of Advisory Committee: Dr. Mustafa Yavuz

This paper briefly describes the theory and methods of x-ray residual stress measurements.

Residual stresses can be defined as the stresses which remain in a material in the absence of any external forces. There are many stress determination methods. Some of those methods are destructive and some are nondestructive. X-ray residual stress measurement is considered as a nondestructive method.

X-ray diffraction together with the other diffraction techniques of residual stress measurement uses the distance between crystallographic planes as a strain gage. The deformations cause changes in the spacing of the lattice planes from their stress free value to a new value that corresponds to the magnitude of the residual stress. Because of Poisson's ratio effect, if a tensile stress is applied, the lattice spacing will increase for planes perpendicular to the stress direction, and decrease for planes parallel to the stress direction. This new spacing will be the same in any similarly oriented planes, with

respect to the applied stress. Therefore the method can only be applied to crystalline, polycrystalline and semi-crystalline materials.

The diffraction angle, 2θ , is measured experimentally and then the lattice spacing is calculated from the diffraction angle, and the known x-ray wavelength using Bragg's Law. Once the d-spacing values are known, they can be plotted versus $\sin^2 \psi$, (ψ is the tilt angle). In this paper, stress measurement of the samples that exhibit a linear behavior as in the case of a homogenous isotropic sample in a biaxial stress state is included. The plot of d vs. $\sin^2 \psi$ is a straight line which slope is proportional to stress. On the other hand, the second set of samples showed oscillatory d vs. $\sin^2 \psi$ behavior. The oscillatory behavior indicates the presence of inhomogeneous stress distribution. In this case the x-ray elastic constants must be used instead of E and ν values. These constants can be obtained from the literature for a given material and reflection combination. It is also possible to obtain these values experimentally. Calculation of the residual stresses for these samples is beyond the scope of this paper and will not be discussed here.

To my Parents

ACKNOWLEDGEMENTS

First of all, I would like to thank my advisor, Prof. Mustafa Yavuz, for being a reference for me whenever I needed. He has been a role model for me and influenced me in almost every aspect of my life.

I would like to thank my co-chair, Prof. Peter McIntyre and committee member Prof. Ibrahim Karaman for their helpful advice throughout my master's program.

I would also like to thank all my friends; Mert Atilhan, Selahattin Aydin, Mustafa Aydin, Suleyman Ciftci, Renat Schaykutdinov, Alparslan Sahin, Osman Cizmeci, Hamza Anderoglu, Daniyar Yusufoglu and many others in College Station for helping me enjoy my life. I would also like to thank Haluk Ersin Karaca, for helping me simply whenever I needed help and turning even the simplest games into a matter of life or death.

I would like to thank all the members of our Intramural Soccer Team. We established such a sincere friendship and had a great time together. Even though we have reached finals several times, we couldn't win a single trophy, yet we have always been champions in the hearts of our beloved ones. Also, the legend barbecue parties at Brandywine will be buried under a noble silence in our hearts. Halo parties in Suveen's apartment were also great times. It was a great pleasure to win against ambitious Mert Atilhan.

Finally, I would like to thank my parents who have trusted me throughout my life. Even though they never went to middle school, they bore and overcame lots of difficulties in order to provide me with a good educational environment. Also, my brother,

Eyup Anderoglu, is thanked for always being one step ahead of me, facing difficulties and sharing his experience with me. His guidance and motivation helped me a lot during my graduate study. It has been always very comfortable to know that I have somebody who can guide me in solving any kind of problem.

TABLE OF CONTENTS

	Page
ABSTRACT.....	iii
DEDICATION.....	v
ACKNOWLEDGEMENTS.....	vi
TABLE OF CONTENTS.....	viii
LIST OF FIGURES.....	x
LIST OF TABLES.....	xii
I. INTRODUCTION.....	1
1.1. Definition.....	1
1.2. The Origin of Stresses.....	2
1.3. Measurement Methods.....	4
1.3.1. Mechanical Stress Measurement Methods.....	4
1.3.1.1. Curvature.....	4
1.3.1.2. Hole Drilling.....	5
1.3.1.3. Compliance Methods.....	5
1.3.2. Magnetic and Electrical Methods.....	5
1.3.3. Ultrasonic Methods.....	7
1.3.4. Thermoelastic Methods.....	7
1.3.5. Photoelastic Methods.....	8
1.3.6. Diffraction Methods.....	8
1.3.6.1. Neutron Diffraction.....	8
1.3.6.2. Synchrotron Diffraction.....	9
II. FUNDAMENTAL CONCEPTS IN X-RAY DIFFRACTION.....	12
2.1. X-ray Source.....	14
2.2. Absorption of X-rays.....	14
2.3. Scattering of X-rays.....	16
2.4. Bragg's Law.....	18
2.5. Diffractometer Geometry.....	21
2.6. Absorption Factor.....	23
2.7. Penetration Depth of X-rays.....	26

	Page
III. CALCULATION OF STRESSES BY X-RAY DIFFRACTION	28
3.1. Brief History of the Method.....	28
3.2. Fundamental Equations.....	28
3.3. Analysis of $d_{\varphi\psi}$ vs. $\sin^2 \psi$ Behavior.....	32
3.3.1. Regular Data	32
3.3.1.1. ψ -Splitting	32
3.3.1.2. Linear $d_{\varphi\psi}$ vs. $\sin^2 \psi$ Behavior (No ψ -Splitting).....	33
3.4. Biaxial Stress Analysis	37
3.4.1. The $\sin^2 \psi$ Method.....	37
3.4.2. The Two-Tilt Method	38
3.5. Triaxial Stress Analysis	39
3.6. Determination of Unstressed d-Spacing	41
IV. EXPERIMENTAL TECHNIQUES.....	43
4.1. Material Under Investigation	44
4.2. Sample Preparation	45
V. RESULTS AND DISCUSSIONS.....	46
5.1. Residual Stress Calculations	47
VI. CONCLUSIONS	59
6.1. Sources of Errors.....	60
6.2. Future Work.....	61
REFERENCES.....	62
VITA.....	64

LIST OF FIGURES

	Page
Figure 1.1 Characteristic residual stress distributions in hardened steel for three different grinding operations.....	3
Figure 2.1a Diffractometer scheme. The incident beam diffracts X-rays of wavelength λ from planes which satisfy Bragg's law. If the surface is in compression then the planes are further apart than in the stress-free state because of Poisson's ratio. The interplanar spacing "d" is obtained from the peak in intensity versus scattering angle and Bragg's law	12
Figure 2.1b When the sample is tilted, diffraction will take place from other grains, but from the same planes (that satisfy Bragg's law). The peak takes place at higher values of 2θ	13
Figure 2.2 Schematic showing the basic components of a modern x-ray tube. Beryllium window is highly transparent to x-rays.....	15
Figure 2.3 Coherent scattering from an electron to a point P.....	17
Figure 2.4 Diffraction of x-rays by a crystal and Bragg's law	19
Figure 2.5 An x-ray diffractometer scheme	22
Figure 2.6 Focusing in the X-ray diffractometer.....	23
Figure 2.7 Diffraction from a flat plane and calculation of the absorption factor	24
Figure 2.8 Geometry of psi-goniometer for the residual stress measurements	25
Figure 3.1 Sample and laboratory coordinate systems.....	29
Figure 3.2a Linear $d_{\phi\psi}$ vs. $\sin^2 \psi$ behavior.....	30
Figure 3.2b ψ -splitting behavior	30
Figure 3.2c Oscillatory behavior of $d_{\phi\psi}$ vs. $\sin^2 \psi$	31

Figure 3.3 Crystal axes and their orientation with respect to laboratory and sample axes	36
Figure 4.1 Bruker-AXS GADDS 2D powder and single-crystal X-Ray diffractometer, Department of Chemistry, Texas A&M University.....	43
Figure 5.1 A linear graph of d vs. $\sin^2 \psi$ fitted to diffraction data with a negative slope	47
Figure 5.2 A linear graph of d vs. $\sin^2 \psi$ fitted to diffraction data with a positive slope	49
Figure 5.3 Two peak values of scattering angle θ are given together with the corresponding d-spacing values for B4.....	51
Figure 5.4a Peak values for $\psi = 15^\circ$ and $\phi = 0^\circ$ of B4.....	53
Figure 5.4b Peak values for $\psi = 15^\circ$ and $\phi = 45^\circ$ of B4.....	53
Figure 5.4c Peak values at $\psi = 30^\circ$ and $\phi = 0^\circ$ of B4.....	54
Figure 5.5a Peaks of all 8 samples are shown for $\Psi=15^0$, $\phi=45^0$	55
Figure 5.5b Peaks for all 8 samples are shown for $\Psi=15^0$, $\phi=00^0$	55
Figure 5.6 The curve exhibits oscillatory behavior.....	57

LIST OF TABLES

		Page
Table 1.1	Comparison of the residual stress measurement techniques.....	11
Table 2.1	Mass absorption coefficients of and densities of some metals for commonly used radiations	16
Table 2.2	Structure factors and reflection conditions	20
Table 4.1	Chemical composition of SS316.....	44
Table 4.2	Physical properties of SS316	44
Table 5.1	The abbreviations of the samples	46
Table 5.2	X-ray diffraction data for B6, $\Psi=30^\circ$ $\phi=90^\circ$	50
Table 5.3	Part of X-ray diffraction data for B2.....	52
Table 5.4	Comparison of two peak data at three different angles of B4.....	54
Table 5.5	Residual stress values of the samples	56
Table 5.6	X-ray elastic constants of some materials.....	58

I. INTRODUCTION

With modern analytical and computational techniques it is usually possible to estimate the stresses that exist in a component. This is not sufficient for the reliable prediction of component performance. Indeed, in many cases where unexpected failure has occurred, this has been due to the presence of residual stresses which seriously shorten component life. Residual stresses can arise from differences in thermal expansivity, yield stress, or stiffness. Considerable effort is currently being devoted to the development of a basic framework within which residual stresses can be incorporated into design in aerospace, nuclear, and other critical engineering industries.

Today, there are a large number of residual stress measurement techniques in use. Some are destructive, while others can be used without significantly altering the component; some have excellent spatial resolution, whereas others are restricted to near-surface stresses or to specific classes of material [1].

1.1 Definition

Residual stress is the stress that exists within a material without application of an external load [2], or it can be described as the stress which remains in a body that is stationary and at equilibrium with its surroundings.

This thesis follows the style and format of Acta Materialia.

1.2 The Origin of Stresses

Residual stresses can arise in materials in almost every step of processing. The origins of residual stresses in a component may be classified as: mechanical, thermal, and chemical. Mechanically generated residual stresses are often a result of manufacturing processes that produce non-uniform plastic deformation. They may develop naturally during processing or treatment, or may be introduced deliberately to develop a particular stress profile in a component. Examples of operations that produce undesirable surface tensile stresses or residual stress gradients are rod or wire drawing, welding, machining and grinding. Fig. 1.1 shows characteristic residual stress profiles resulting from 3 different types of grinding. It can be seen that conventional and highly abrasive grinding produced tensile stresses near the surface compared with compressive stresses with gentle grinding. Compressive residual stresses usually lead to performance benefits and can be introduced by shot peening, toughening of glass or cold expansion of holes. On a macroscopic level, thermally generated residual stresses are often the consequence of non-uniform heating or cooling operations. Coupled with the material constraints in the bulk of a large component this can lead to severe thermal gradients and the development of large internal stresses. An example is the quenching of steel or aluminum alloys, which leads to surface compressive stresses, balanced by tensile stresses in the bulk of the component.

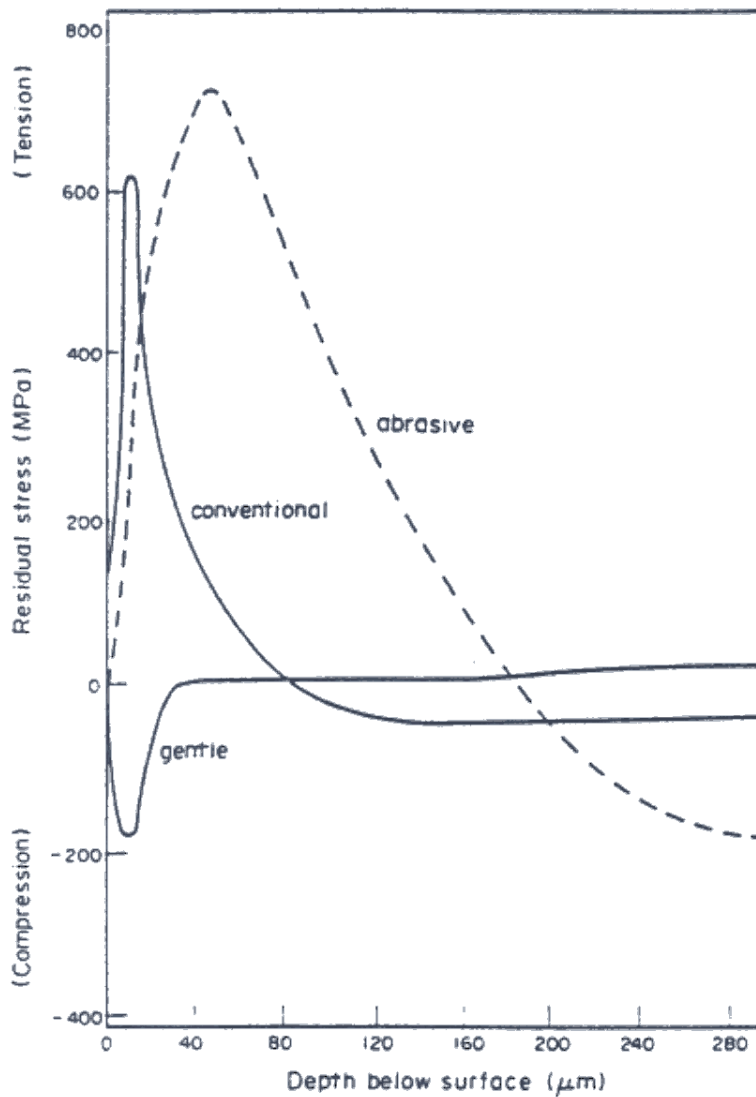


Figure 1.1. Characteristic residual stress distributions in hardened steel for three different grinding operations [3].

The chemically generated stresses can develop due to volume changes associated with chemical reactions, precipitation, or phase transformation. Chemical surface treatments and coatings can lead to the generation of substantial residual stress gradients

in the surface layers of the component. Nitriding produces compressive stress in the diffusion region because of expansion of the lattice and precipitation of nitrides, and carburizing causes a similar effect. The magnitude of residual stresses generated in coatings can be very high –compressive stresses of the order of 6-8GPa or higher have been measured at the interface of some thermal barrier coatings (TBCs).

1.3 Measurement Methods

1.3.1. Mechanical Stress Measurement Methods

These methods based on the monitoring of changes in component distortion, either during the generation of the residual stress, or afterwards, by deliberately removing material to allow the stress to relax.

1.3.1.1. Curvature

These methods are usually used to determine the stress within coatings and layers. The deposition of a layer can make the substrate to bend.

The changes in curvature during deposition make it possible to calculate variations in stress as a function of deposit thickness.

Curvature measurements can also be used to determine the stresses by incremental layer removal. This has been used for metallic and polymeric composites, and for thin coatings produced using chemical and physical vapor deposition (CVD and PVD). Since the stress distribution associated with a given curvature is not unique, there is some ambiguity in this latter approach.

1.3.1.2. Hole Drilling

The undisturbed portions of a stressed sample will relax into a different shape when the locality is machined; this provides data for the calculation of residual stress. The machining operation is simply drilling a hole around which the strain is measured.

Although it is possible to infer the variation in stress with depth by incrementally deepening the hole, it is difficult to obtain reliable measurements when the depth is beyond the size of diameter. This method is cheap and widely used. If the residual stresses exceed 50% of the yield stress, localized yielding could introduce some errors. Although the method is used for coatings, it is not practical for thin ($<100\mu\text{m}$), or brittle coatings.

1.3.1.3. Compliance Methods

The crack compliance method is basically cutting a small slot to see the relaxation of stress in the vicinity of the crack using strain gauge interferometry. Increasing the depth of the slot will allow resolving the stress field normal to the crack as a function of depth for relatively simple stress distributions.

1.3.2. Magnetic and Electrical Methods

There are two magnetic methods: the magnetostriction and the Barkhausen noise. The former based on the measurement of permeability and magnetic induction, the latter on the analysis of magnetic domain wall motion.

If magnetostrictive materials are stressed the preferred domain orientations are altered. This makes domains most nearly oriented to a tensile stress to grow (positive magnetostriction) or shrink (negative magnetostriction). Stress induced magnetic anisotropy causes the rotation of an induced magnetic field away from the applied

direction. It is possible to monitor these small rotations in the plane of the component surface by a sensor coil. If there is no rotation, then the principal axes of the magnetic field and stress are parallel. When the assembly is rotated, both the principal stress directions and the size of the principal stress difference can be measured. Magnetoacoustic emission is the generation of elastic waves caused by changes in magnetostrictive strain during the movement of magnetic domain walls and is generally detected from the material bulk. Barkhausen emission on the other hand, is recorded as a change in the emf proportional to the rate of change in magnetic moment detected in probe coils as domain walls move. It is attenuated at high frequencies by eddy current shielding and so provides only a near surface probe ($<250 \mu\text{m}$). Magnetic methods have the advantage of providing cheap and portable methods for non-destructive residual stress measurement.

Eddy current techniques can simply be described as inducing eddy currents in the material under test and detecting changes in the electrical conductivity or magnetic permeability through changes in the test coil impedance. The depth of penetration can be changed by altering the excitation frequency, but is around 1 mm at practical frequencies, and the probe cannot identify the direction of the applied stress. Recent studies on this method showed that eddy current methods can be applied to a wider range of materials than magnetic methods. Although eddy current methods are not well suited to basic measurements of residual stress due to the sensitivity of eddy current monitoring to plastic work and microstructural changes, they can provide a quick and cheap inspection method.

1.3.3. Ultrasonic Methods

Changes in ultrasonic speed can be observed when a material is subjected to a stress, the changes providing a measure of the stress averaged along the wave path. The acoustoelastic coefficients necessary for the analysis are usually calculated using calibration tests. Different types of wave can be employed but the commonly used technique is the critically refracted longitudinal wave method. The greatest sensitivity is obtained when the wave propagates in the same direction as the stress [1]. The basic equation for the stress calculation;

$$V = V_0 + K\sigma \quad (1.1)$$

where V_0 the velocity of a wave is in an unstressed medium, σ is the stress and K is a material parameter known as acoustoelastic constant [5].

1.3.4. Thermoelastic Methods

The elastic deformations in the materials cause small changes in temperature (1 mK for 1 MPa in steel). It is possible to map the thermal variations using an infrared camera. These variations are indications of variations in stress. The thermoelastic constant (β) describes the dependence of temperature on stress. Using the thermoelastic constant the hydrostatic stress component can be determined using the relation

$$heat \approx -\beta \frac{\partial}{\partial T} (\sigma_{11} + \sigma_{22} + \sigma_{33}) \quad (1.2)$$

This method is usually used in fatigue studies. Since the method uses infrared cameras, it is effected by the sensitivity of them hence has limited use in present [1].

1.3.5. Photoelastic Methods

The speed of light is prone to vary unisotropically in transparent materials, when the material is subjected to stress. This tendency is called photoelastic effect.

It gives rise to interference fringe patterns when such objects are observed in white or monochromatic light between crossed polars. It is possible to interpret the resulting fringe patterns to give the local maximum shear stress when the stress optic coefficient n is known from a calibration experiment

$$\sigma_{11} - \sigma_{22} = \frac{fn}{t} \quad (1.3)$$

where σ_{11}, σ_{22} are in plane principal stresses, f is the fringe order, and t is the optical path length. Photoelastic measurements are generally made using two-dimensional epoxy resin models or from slices cut from three-dimensional models in which the stresses have been frozen in [1].

1.3.6. Diffraction Methods

1.3.6.1. Neutron Diffraction

Neutron diffraction is a non-destructive method of determination of residual stresses in crystalline materials. Neutron diffraction provides the values of elastic strain components parallel to the scattering vector which can be converted to stress. Neutron diffraction measures strain components from changes in crystal lattice spacing. When crystalline materials exposed to radiation of wavelength close to interplanar spacing ($0.5\text{-}3 \text{ \AA}$) elastically and coherently scatter this radiation as distinctive Bragg peaks

imaged usually by a position sensitive detector. The angle at which any given peak occurs can be calculated using Bragg's equation

$$2d_{hkl} \sin \theta_{hkl} = \lambda \quad (1.4)$$

where λ is the wavelength of the radiation, d_{hkl} is the lattice plane spacing of a family of crystallographic planes (hkl) responsible for the Bragg peak and θ_{hkl} is the angular position of this diffraction peak. The peak will be observed at an angle of $2\theta_{hkl}$ from the incident beam. If a specimen is elastically strained, the lattice spacing changes. Therefore any elastic strain will be apparent as a shift in the value of $2\theta_{hkl}$ for a particular reflecting plane illuminated by a fixed wavelength. By differentiating the Bragg's equation,

$$\Delta\theta_{hkl} = -(\Delta d / d_0) \tan \theta_0 \quad (1.5)$$

where Δd is the change of lattice spacing, and d_0 , the lattice spacing of a stress-free sample of the material. So, the strain in the (hkl) set of planes can be calculated with

$$\varepsilon = (\Delta d / d_0) = -\Delta\theta \cot \theta_0 \quad (1.6)$$

The direction in which strain is measured is along the scattering vector and is perpendicular to the diffracting planes [6-7].

1.3.6.2. Synchrotron Diffraction

Synchrotrons (hard X-rays), provide very intense beams of high energy X-rays. These X-rays have higher depth penetration than conventional X-rays (~50 mm in Al). This increased penetration depth means that synchrotron diffraction is capable of providing high spatial resolution, three-dimensional maps of the strain distribution to millimeter

depths in engineered components. Higher penetration depth is considered as one of the major advantages of synchrotron diffraction over the conventional X-ray diffraction. Another advantage is that intense narrow beams of 1 mm-10 μm in size are possible. This leads to spatial resolutions that are limited by the crystallite size within the sample not by the instrument. The measurement is also much quicker than the conventional X-ray diffraction. Today synchrotron diffraction is only available at some central facilities, in much the same way as with neutron diffraction [3-1].

Table 1.2 shows comparison of the residual stress measurement techniques.

Table 1.2. Comparison of the residual stress measurement techniques [3-1].

Technique	PROs	CONs
X Ray Diffraction	Versatile, widely available Wide range of materials Portable systems Macro and micro RS*	Basic measurements Lab-based systems, small components
Hole Drilling	Quick, simple, Widely available Portable. Wide range of materials Deep hole drilling for thick section components	Interpretation of data Destructive Limited strain sensitivity and resolution
Synchrotron	Improved penetration & resolution of X-rays Depth profiling Fast Macro and micro RS	Specialist facility only Lab-based
Neutron Diffraction	Excellent penetration & resolution 3D maps Macro and micro RS	Specialist facility only Lab-based
Magnetic	Very fast Wide variety of magnetic techniques Portable	Only ferromagnetic materials Need to separate the microstructure signal from that due to stress
Ultrasonic	Generally available Very fast Low cost Portable	Limited resolution Bulk measurements over whole volume
Raman/Fluorescence	High resolution Portable systems available	Surface measurements Interpretation Calibration Limited range of materials

*RS: Residual stress

II. FUNDAMENTAL CONCEPTS IN X-RAY DIFFRACTION

Diffraction methods of residual stress determination basically measure the angles at which the maximum diffracted intensity take place when a crystalline sample is subjected to x-rays. From these angles it is possible to obtain the interplanar spacing of the diffraction planes using Bragg's law. If the residual stresses exist within the sample, then the d spacing will be different than that of an unstressed state. This difference is proportional to magnitude of the residual stress.

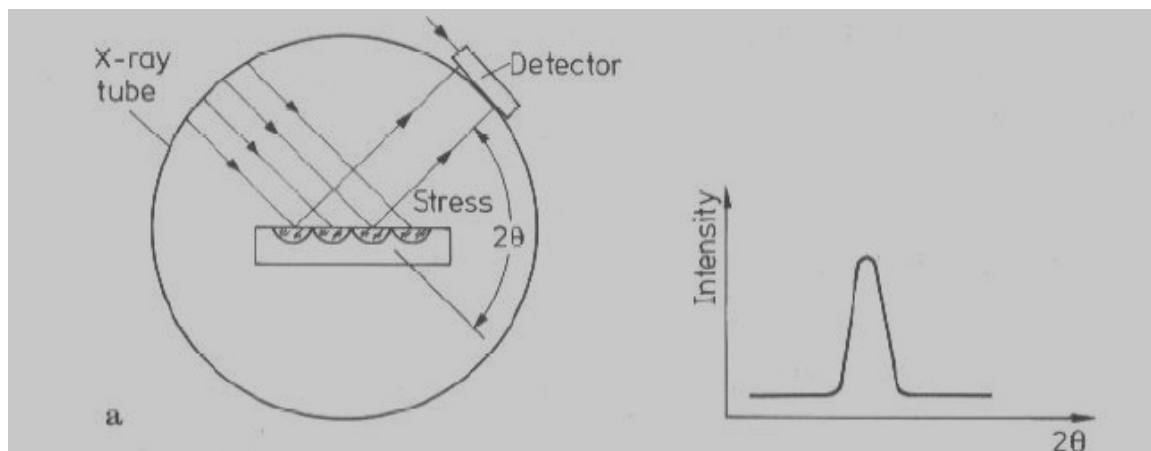


Figure 2.1a. Diffractometer scheme. The incident beam diffracts X-rays of wavelength λ from planes which satisfy Bragg's law. If the surface is in compression then the planes are further apart than in the stress-free state because of Poisson's ratio. The interplanar spacing " d " is obtained from the peak in intensity versus scattering angle and Bragg's law [6].

With reference to Figure 2.1a, assume that the detector is turned over a range of angles, 2θ , to find the angle, θ , of the diffraction from grains which satisfy Bragg's law. In other words the grains that have planes of atoms with interplanar spacing "d" such that $\lambda = 2d \sin \theta$. The grains that have planes with this spacing that are parallel to the surface will diffract as in Figure 2.1a. This diffraction occurs from a thin surface layer which is about $20 \mu\text{m}$. If the surface is in compression, then the interplanar spacing "d" is larger than in the stress free state as a result of Poisson's effect. When the specimen is tilted with respect to the incoming beam new grains will diffract and the orientation of the diffraction planes is more nearly perpendicular to the stress direction (Figure 2.1b).

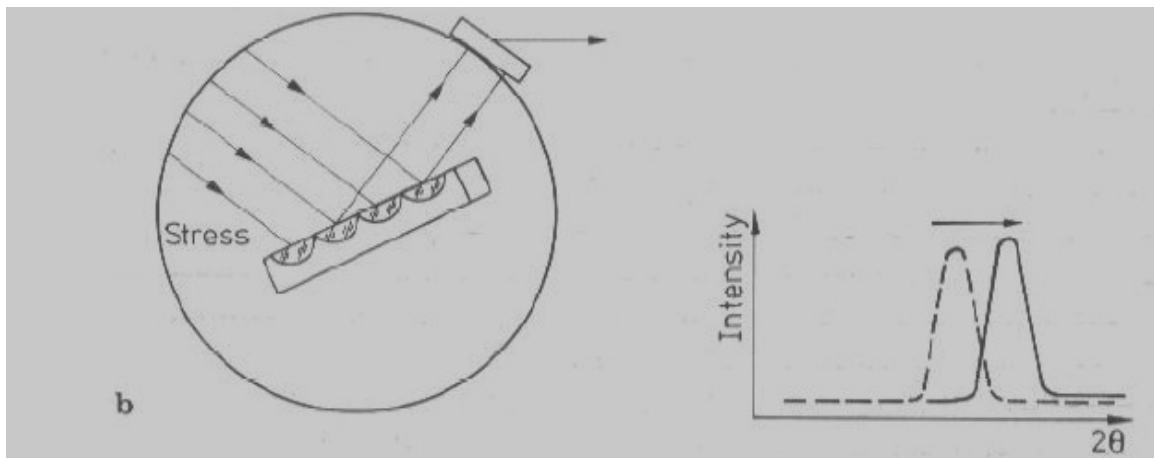


Figure 2.1b. When the sample is tilted, diffraction will take place from other grains, but from the same planes (that satisfy Bragg's law). The peak takes place at higher values of 2θ . [6]

As a result of the tilt, the d spacing decreases and the angle 2θ increases, as seen in the figures. In this case the d spacing acts as a strain gauge. Because of the fact that

the interplanar spacing is so small, both micro and macro stresses will effect it. The XRD measures sum of all these stresses.

2.1. X-ray Source

In early 1895, W. C. Roentgen (1845-1923) discovered that if the electrons are accelerated by a high voltage in a vacuum tube and allowed to strike a glass or metal surface, fluorescent minerals some distance away would glow, and film would become exposed. He attributed these effects to a new type of radiation which are different from cathode rays. They were given the name X-rays which means an unknown quantity. X-rays are produced similar to Roentgen's today [7].

X-rays are produced in a standard way: by accelerating electrons with a high voltage and allowing them to collide with a metal target. Electrons are produced by heating a tungsten filament cathode in a vacuum. The cathode is as a high negative potential, and the electrons are accelerated toward the anode, which is at ground potential. Then the electrons hit the anode with a very high velocity. The loss of energy as a result of the impact is manifested as x-rays.

2.2. Absorption of X-rays

X-rays are attenuated when they pass through matter, thus the transmitted beam is weaker than the incident beam. Many different processes cause the decrease in the incident beam. Scattering (coherent & incoherent), heat production or excitations of photoelectrons, etc. are some of the contributors. The total loss in the intensity is termed absorption. The attenuation related to thickness of an infinitesimal slab is given by the relation

$$\frac{dI}{I} = -\mu dz \quad (2.1)$$

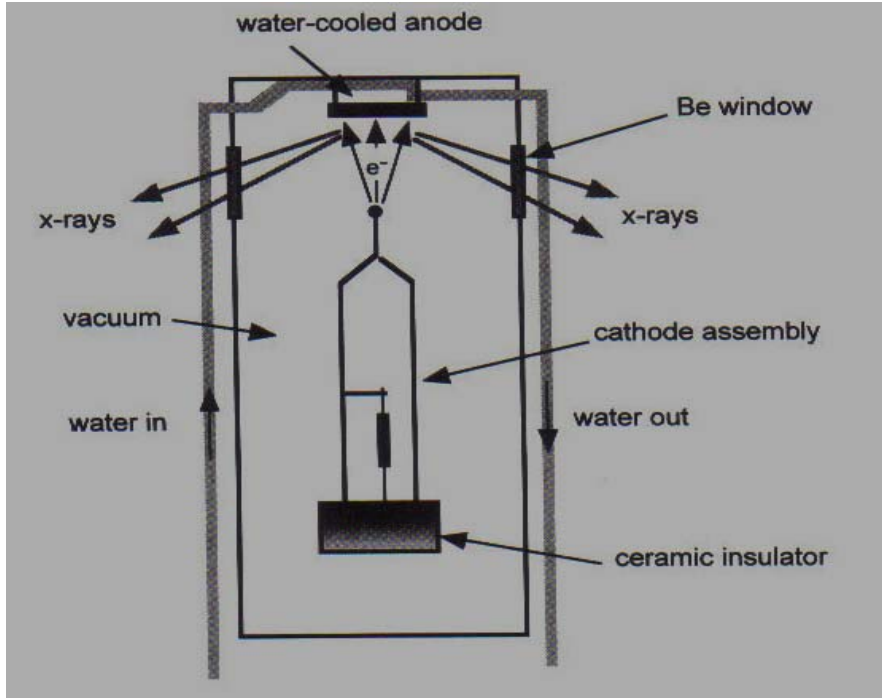


Figure 2.2. Schematic showing the basic components of a modern x-ray tube. Beryllium window is highly transparent to x-rays. [8-9]

where I is the intensity of the transmitted beam, μ is the linear absorption coefficient. It is proportional to density and is usually listed as $(\frac{\mu}{\rho})$. This ratio is known as mass absorption coefficient. It is a material property and independent of the material phase. Mass absorption coefficients of some materials are given in Table 2.1. Equation 2.1 can be integrated (for a homogenous finite slab thickness of z) to give

$$I_z = I_0 e^{(-\mu/\rho)\rho z} \quad (2.2)$$

where I_0 is the intensity of the incident beam [6, 10].

Table 2.1. Mass absorption coefficients of and densities of some metals for commonly used radiations [6].

Metal	Density (gm/cm ³)	Mo K α ($\lambda=0.711 \text{ \AA}$)	Cu K α ($\lambda=1.542 \text{ \AA}$)	Co K α ($\lambda=1.790 \text{ \AA}$)	Cr K α ($\lambda=2.290 \text{ \AA}$)
Aluminum	2.70	5.30	48.7	73.4	149
Iron	7.87	38.3	324	59.5	115
Nickel	8.90	47.7	49.3	75.1	145
Copper	8.96	49.7	52.7	79.8	154
Titanium	4.54	23.7	204	304	603

2.3. Scattering of X-rays

When a beam of x-rays is incident on the specimen, the photons collide with the electrons and scatter in different directions. There are two types of collisions. First type is elastic and the second one is inelastic. The former is the case when the x-rays collide with the electrons that are tightly bound to nucleus (usually the inner orbital electrons). There is no momentum transfer between the photon and electron which means scattered photon has the same energy and wavelength after the collision. This type of scattering is called coherent scattering (Figure 2.3). On the other hand, for the inelastic collision there is a momentum transfer from photon to electron. Due to this momentum transfer, photon loses energy and has longer wavelength. In the former there is a relation between

phases of incident and scattered x-rays, whereas this is not the case for the latter. Latter is called Compton modified scattering or Incoherent scattering. In both cases the photons are scattered in all directions.

When an unpolarized x-ray beam impinges on an electron, the total scattered intensity on a point P is given by the equation

$$I = I_0 \frac{e^4}{r^2 m^2 c^4} \left(\frac{1 + \cos^2 2\theta}{2} \right) \quad (2.3)$$

where I_0 is the intensity of the incoming beam, m is the electron mass, c is the speed of light, e is the electron charge, r is the length of the position vector to point P, and 2θ is the angle between r and the incident beam direction. The term $(1 + \cos^2 2\theta)$ is called polarization factor.

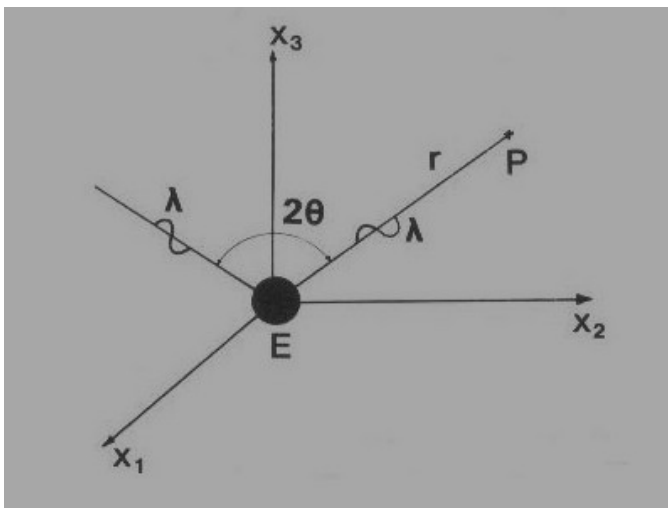


Figure 2.3. Coherent scattering from an electron to a point P [6].

Equation 2.3 is for an electron. If there are Z electrons (referring to atomic number Z), there will be Z beam sources at different positions. That means Z rays all with λ will arrive at point P. It is also important to note that the total scattering intensity is the some of relative phases of all individual rays. For instance if all the beams are in phase the total intensity will be $Z^2(I_e)$, where I_e is given by equation 2.3. For any other direction, the beams from every single electron will be out of phase by different amounts and a certain amount of destructive interference take place. Hence only coherence scattering can take part in this process.

The total coherent scattering factor from an atom to a point P is called atomic scattering factor (f) is defined as

$$f = \frac{\text{amplitude of wavescattered by an atom}}{\text{amplitude of wave scattered by an electron}} \quad (2.4)$$

f is equal to Z at 2θ equal to 0, and decreases as 2θ increases. Tabulated values of atomic scattering factors for elements can be obtained from references [12-13].

2.4. Bragg's Law

In real materials there are a great many atoms. When atoms spaced at regular intervals are irradiated by X-ray beams, the scattered radiation undergoes interference. In certain directions constructive; in other directions destructive interference occurs depending on the spacing between planes, and the wavelength of the incident radiation. The law that governs constructive interference (diffraction) is known as Bragg's law. When x-rays strikes a crystal, the beam is reflected not only from the surface atoms but also from the atoms underneath the top surface to some considerable depth (Figure 2.4) [6-14].

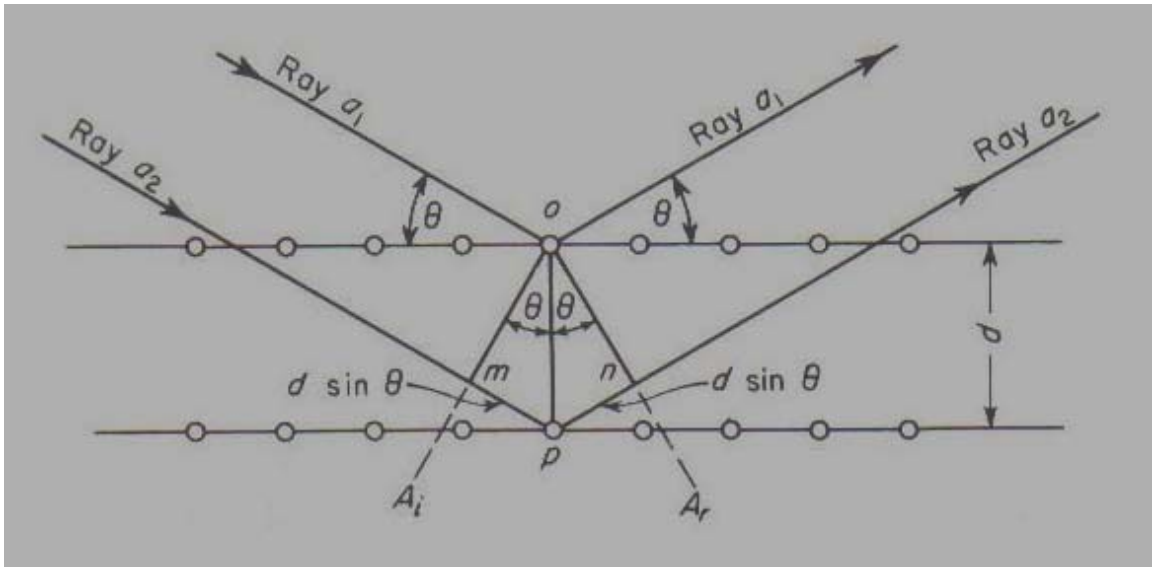


Figure 2.4. Diffraction of x-rays by a crystal and Bragg's law [14].

Figure 2.4 shows reflection of an x-ray beam from two parallel lattice planes. In real there would be too many other planes. In the figure, the distance between two parallel planes is represented by “d” (interplanar spacing). Lines A_i and A_r are drawn perpendicular to incident and reflected beams respectively. The line oA_i is a wave front. Points o and m must be in phase because they lie on this line. The same condition is valid for points o and p . This condition can be satisfied when the distance mpn equals a multiple of a complete wavelength. That is to say it must equal $n\lambda$ where n is an integer and λ is wavelength of x-rays.

From the figure, the distances mp and np equal $d \sin \theta$. The distance mpn is $2d \sin \theta$. When this quantity equated to $n\lambda$ we have:

$$n\lambda = 2d \sin \theta \quad (2.5)$$

where $n = 1, 2, 3, \dots$, λ is wavelength, d is interplanar spacing, θ is angle of reflection.

This equation is known as Bragg's law.

When the relation is satisfied, the reflected rays a_1 and a_2 will be in phase which results in constructive interference.

The three-dimensional symmetry of the unit cell was not taken account into consideration in the derivation of Bragg's law. Due to the particular positions of the atoms in the unit cell Bragg's law is necessary but not sufficient condition for diffraction. The total diffraction intensity from a unit cell can be determined by summing up the waves from each atom. If the scattering amplitude from the i_{th} atom, with fractional dimensionless coordinates u_i, v_i, w_i , is f_i , the relative intensity scattered by the unit cell for a given reflection hkl is proportional to

$$F_{hkl} = \sum_{i=1}^N f_i e^{2\pi i(hu_i + kv_i + lw_i)} \quad (2.6)$$

The term F_{hkl} is called structure factor and describes the effect of the crystal structure on the intensity of the diffracted beam. Using equation 2.6 structure factors of some simple Bravais lattice types are shown in Table 2.2.

Table 2.2. Structure factors and reflection conditions [6].

Bravais lattice	Structure factor	Reflections present	Reflections absent
Simple	$F=f$	all	None
Body-centered	$F=f(1+e^{\pi i(h+k+l)})$	$(h+k+l)$ even	$(h+k+l)$ odd
Face-centered	$F=f(1+e^{\pi i(h+k)}+e^{\pi i(h+l)}+e^{\pi i(l+k)})$	h,k,l unmixed	h,k,l mixed

As a result the conditions for diffraction can be summarized as follows

- Bragg's law is satisfied for one or more sets of crystallographic plane (hkl).
- The structure factor F for these hkl reflections are non-zero for the unit cell.

By using a monochromatic x-ray beam of known wavelength and measuring the diffraction angle 2θ , it is possible to determine interplanar spacing d_{hkl} . This technique is the basis of structure analysis and of residual stress measurement.

Residual stress/strain analysis together with the other structure analysis methods is based on Bragg's law, and therefore there are some implicit assumptions:

- 1- The x-rays accepted as traveling waves.
- 2- The path difference between the waves arriving at a point is a linear function of interplanar spacing d .
- 3- The scattering is elastic and energy is conserved during collision. That means there is no phase difference between incident and diffracted beams.
- 4- The scattered waves within the specimen do not rescatter.

The above assumptions are the basis of the kinematic theory of diffraction. Now we can move on to the methods and the equipment necessary for residual stress measurements by x-ray diffraction.

2.5. Diffractometer Geometry

The diffractometer is the most common apparatus used for determining diffraction patterns. The diffractometer uses electronic counters sensitive to x-rays, rotation tools to rotate the sample, and a detector to measure x-ray intensities. In Figure 2.5 the basic geometry of an x-ray diffractometer is shown. X-rays coming from an x-ray source strike the specimen which is stabilized by a sample holder. The sample holder can be

rotated around X axis perpendicular to the plane of the diffractometer. Then the diffracted beam is detected by a suitable detector. The detector can be rotated around X along the circumference of the diffractometer. The rotation of the sample holder and detector can be determined very accurately (± 0.005 to $\pm 0.0005^\circ$)

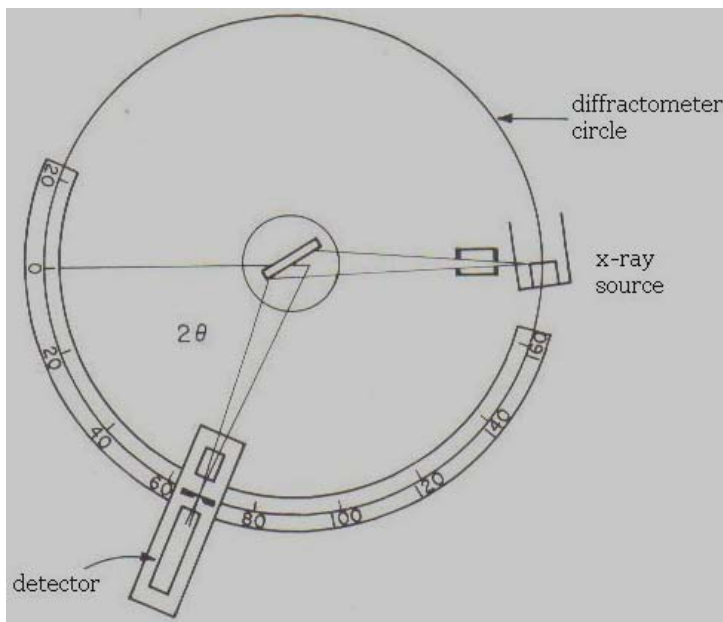


Figure 2.5. An x-ray diffractometer scheme [6].

The detector is moved along with the diffractometer circle to detect the diffracted beam (Figure 2.5). The sample holder is also rotated around X half of the rotation angle of the detector simultaneously for the sake of keeping the focus (Figure 2.6).

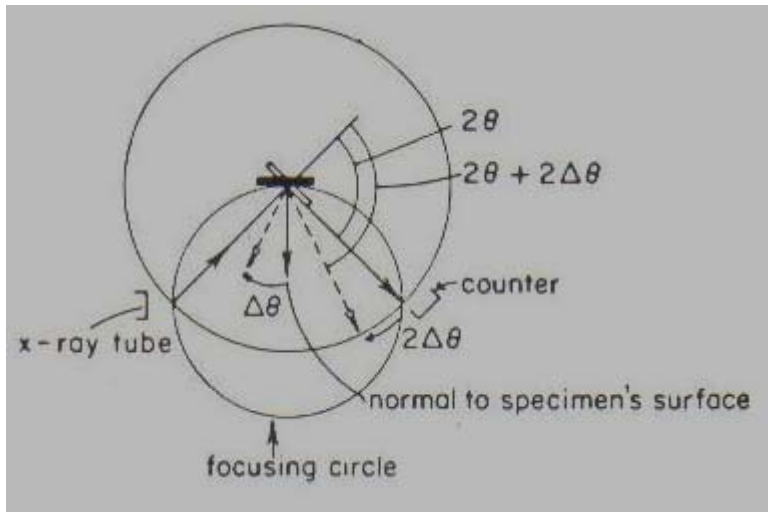


Figure 2.6. Focusing in the X-ray diffractometer [6].

Since both sets of rays section equal arcs on the focusing circle, the divergence in the incident beam will converge (focus) at the receiving slit.

The detection surface of the diffractometer is a cylindrical segment of radius R (radius of the diffractometer) and height l (the length of the receiving slit). The detector only perceives the intersection of the diffracted beam with the surface. As a result, optimization of angular resolution with intensity results in a rectangular slit (generally).

2.6. Absorption Factor

The path of x-ray beam identical from one volume element to another in a flat sample may vary remarkably in a specimen with complex geometry (such as a curved one), leading to phenomena called absorption effect [5]. In this part the most common situation, absorption in a flat sample will be studied.

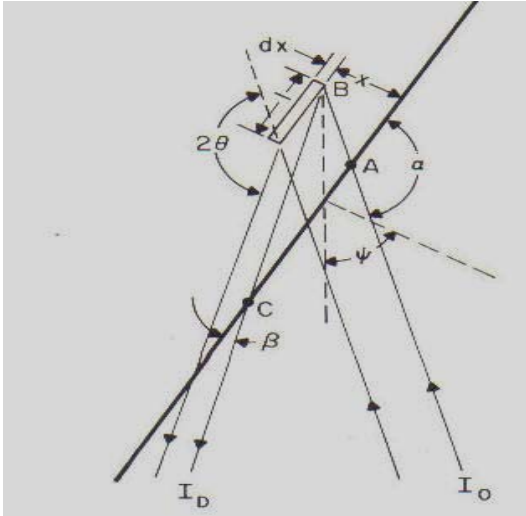


Figure 2.7. Diffraction from a flat plane and calculation of the absorption factor [6].

Suppose an x-ray beam of intensity I_0 strikes a flat sample with an angle (Figure 2.7). Because of the absorption the total energy reaching a layer of length l and thickness dx , located at depth x below the surface, is proportional to $(aI_0e^{-\mu AB})$ where a is the volume fraction (of crystallites) that can diffract at this angle. The total energy diffracted by this layer is $ablI_0e^{-\mu AB} dx$, where b is the fraction of incident beam energy diffracted by unit volume. The intensity of the diffracted beam also decreases when it traverses the distance BC by a factor $e^{-\mu BC}$. Hence the total diffracted intensity becomes

$$dI_D = abI_0e^{-\mu(AB+BC)} dx \quad (2.7)$$

Making necessary substitutions from the figure and integrating the equation for an infinitely thick specimen gives the total diffracted intensity

$$I_D = \frac{I_0 ab}{2\mu} (1 - \tan \psi \cot \theta) \quad (2.8)$$

For the particular geometry, the angular dependence of the absorption factor is given by the term $(1 - \tan \psi \cot \theta)$.

Note that for the values of $\psi < 0$ the absorption factor becomes $1 + \tan(|\psi|) \cot \theta$.

Equation 2.8 tells that for $\psi = 0$ no matter what the θ is, the value of the absorption factor is 1. Hence there is no absorption correction for the data obtained.

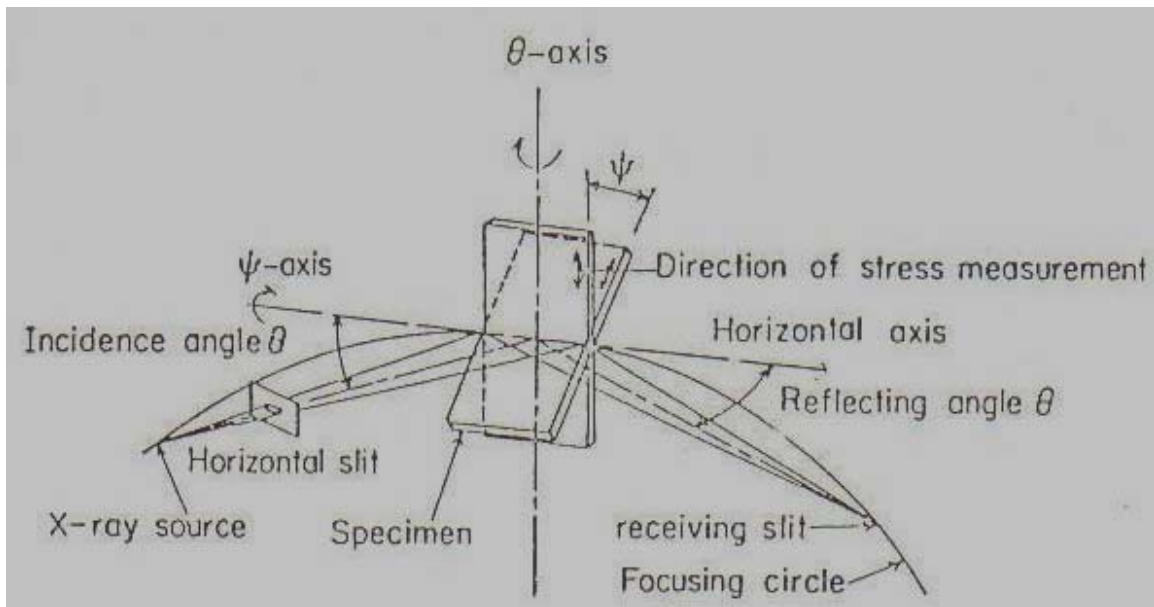


Figure 2.8. Geometry of psi-goniometer for the residual stress measurements [6].

On the other hand, if $G_x = 1 - \exp(-2\mu x / \sin \theta)$ which is the case during residual stress measurements, a correction may be necessary. The geometry shown in Figure 2.8 is known as the psi-goniometer. The geometry shows that the tilts are around an axis parallel to the plane of the diffractometer. The incident and the diffracted beams traverse

the same distance independent of the ψ -tilts. Hence, in this case there will be no absorption correction.

2.7. Penetration Depth of X-rays

The attenuation due to absorption limits the x-ray penetration depth. The penetration depth depends on the absorption coefficient of the material and the beam dimensions on specimen surface. Because attenuation of the incident beam is proportional to the thickness of the material it passes through, the contribution to the diffracted beam from layers deeper down in the material within the irradiated volume is less. Also because the diffracted beam has to traverse more material before leaving the surface, there will be more attenuation.

The intensity of an x-ray beam diffracted from an infinitesimally thin layer located a distance x below the surface is given by (making necessary geometrical substitutions in equation 2.7)

$$dI_D = \frac{I_0 ab}{\sin(\theta + \psi)} \exp \left\{ -\mu x \left[\frac{1}{\sin(\theta + \psi)} + \frac{1}{\sin(\theta - \psi)} \right] \right\} dx \quad (2.9)$$

Then the total intensity diffracted by the volume of the material between this layer and the surface is given by

$$G_x = \frac{\int_{x=0}^x dI_D}{\int_{x=0}^{\infty} dI_D} = 1 - \exp \left\{ -\mu x \left[\frac{1}{\sin(\theta + \psi)} + \frac{1}{\sin(\theta - \psi)} \right] \right\} \quad (2.10)$$

for $\psi = 0$ becomes

$$G_x = 1 - \exp(-2\mu x / \sin \theta) \quad (2.11)$$

Equation 2.11 shows us that the effective depth of penetration can be defined as the thickness that contributes 99% of the diffracted intensity. For instance effective depth of penetration for steel is approximately 5.4 microns [6,15].

It can be said from the equations that the effective depth of penetration is also a function of the ψ , which decreases with increasing ψ . This effect is taken account into consideration for residual stress calculations.

III. CALCULATION OF STRESSES BY X-RAY DIFFRACTION

In this section the concepts related to x-ray diffraction which was studied in the previous sections will be combined in the derivation of the equations of the residual stress. It is important to note that stress is not measured directly by the x-ray diffraction; it is always strain that is measured. Then the stress is calculated using appropriate equations of elasticity.

3.1. Brief History of the Method

This method was first proposed by Lester and Aborn in 1925. In 1930, Sachs and Weerts showed that the accuracy obtained was similar to other methods. The method was improved in 1934 by Barret and Gensamer which was used to measure sum of eigenstresses. In 1935, Glocker showed that it was possible to evaluate each of the eigenstresses [5]. Since then, because of both technological improvements and better understanding of the deformation of the crystal lattice, especially influence of anisotropy and crystallographic texture, a remarkable progress made on the method. Today, it is one of the most common techniques that is used to measure residual stresses.

3.2. Fundamental Equations

In Figure 3.1 the orthogonal coordinate systems used to derive equations are shown. The axes \underline{S}_i are for the surface of the sample with \underline{S}_1 and \underline{S}_2 on the surface. \underline{L}_i define the laboratory system with \underline{L}_3 is in the direction of the normal to the planes (hkl) whose interplanar spacing d will be measured. \underline{L}_2 makes an angle ϕ with \underline{S}_2 and is in the plane which is defined by \underline{S}_1 and \underline{S}_2 . When the interplanar lattice spacing d is obtained from the

diffraction peak for a given reflection hkl , the strain component along \underline{L}_3 can be obtained using the formula

$$(\varepsilon'_{33})_{\phi\psi} = \frac{d_{\phi\psi} - d_0}{d_0} \quad (3.1)$$

where d_0 is the unstressed interplanar spacing.

(Primed components refer to laboratory system \underline{L}_i whereas unprimed components refer to the sample coordinate system, \underline{S}_i)

The strain in equation 3.1 can be transformed to the sample coordinate system using tensor transformation [16]

$$(\varepsilon'_{33})_{\phi\psi} = a_{3k}a_{3l}\varepsilon_{kl} \quad (3.2)$$

where a_{3k}, a_{3l} are the direction cosines between $\underline{L}_3, \underline{S}_k$ and $\underline{L}_3, \underline{S}_l$.

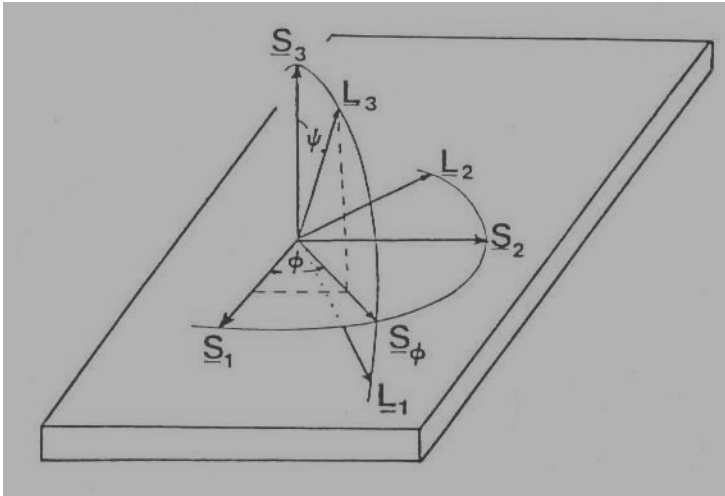


Figure 3.1. Sample and laboratory coordinate systems [6].

Then the direction cosine matrix will be

$$a_{ik} = \begin{vmatrix} \cos \phi \cos \psi & \sin \phi \cos \psi & -\sin \psi \\ -\sin \phi & \cos \phi & 0 \\ \cos \phi \sin \psi & \sin \phi \sin \psi & \cos \psi \end{vmatrix} \quad (3.3)$$

substitute a_{3k} , a_{3l} in equation 3.2 to get

$$\begin{aligned} (\varepsilon'_{33})_{\phi\psi} = \frac{d_{\phi\psi} - d_0}{d_0} = & \varepsilon_{11} \cos^2 \phi \sin^2 \psi + \varepsilon_{12} \sin 2\phi \sin^2 \psi + \varepsilon_{22} \sin^2 \phi \sin^2 \psi \\ & + \varepsilon_{33} \cos^2 \psi + \varepsilon_{13} \cos \phi \sin 2\psi + \varepsilon_{23} \sin \phi \sin 2\psi \end{aligned} \quad (3.4)$$

Equation 3.4 is the fundamental equation that is used in x-ray diffraction strain measurement.

As a result of x-ray diffraction, there are three basic behaviors of $d_{\phi\psi}$ vs. $\sin^2 \psi$ for a d-spacing at all psi tilts. Now we will study the three patterns as shown in Figures 3.2a, b and c.

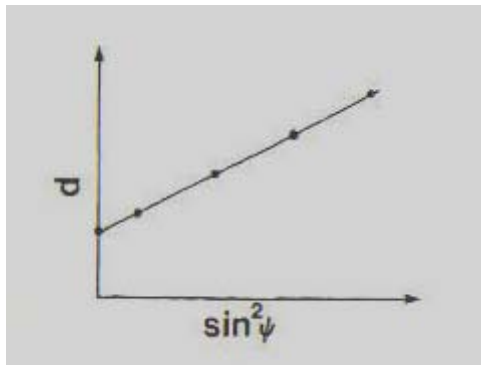


Figure 3.2a. Linear $d_{\phi\psi}$ vs. $\sin^2 \psi$ behavior.

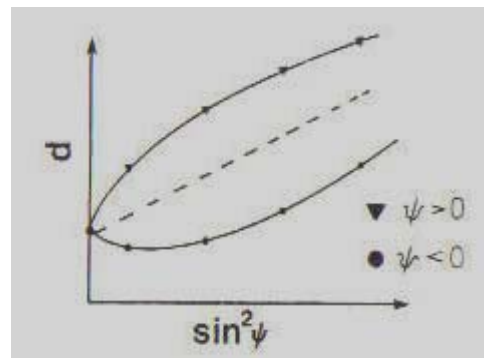


Figure 3.2b. ψ -splitting behavior.

The graphs in Figures 3.2a and b shows regular $d_{\phi\psi}$ vs. $\sin^2 \psi$ pattern. For both cases equation 3.4 can be used to determine the strains from the given data. Equation 3.4 tells that if ε_{13} and ε_{23} are both zero, then there is a linear behavior of $d_{\phi\psi}$ vs. $\sin^2 \psi$ which is shown in Figure 3.2a. On the other hand, if either or both of these components are non-zero, values of d measured at positive and negative ψ tilts will be different because of the term $\sin 2\psi$. As a result, $\sin 2\psi$ will cause a split (Figure 3.2b) in the associated $d_{\phi\psi}$ vs. $\sin^2 \psi$ behavior, which is named “ ψ -splitting” [6].

The third type of $d_{\phi\psi}$ vs. $\sin^2 \psi$ behavior exhibits oscillatory pattern (Figure 3.2c). Further modification should be done on the equation 3.4. That will be discussed later on.

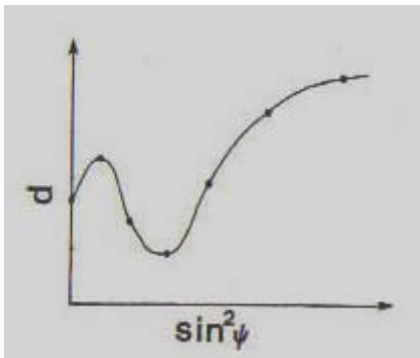


Figure 3.2c. Oscillatory behavior of $d_{\phi\psi}$ vs. $\sin^2 \psi$ [6]. This type of data can not be solved with the equation 3.4.

3.3. Analysis of $d_{\phi\psi}$ vs. $\sin^2 \psi$ Behavior

3.3.1. Regular Data

3.3.1.1. ψ -Splitting

There are six unknown strains ($\varepsilon_{11}, \varepsilon_{12}, \varepsilon_{22}, \varepsilon_{33}, \varepsilon_{13}, \varepsilon_{23}$) in the equation 3.4. There should be six independent equations to determine these six strains. That is, the equation can be solved by measuring $d_{\phi\psi}$ in six independent directions. In practice, for the sake of improving accuracy more points are measured. For instance, suppose that the data exhibits “ ψ -splitting”, then the solution is given as follows;

$$a_1 = \frac{1}{2} [\varepsilon_{\phi\psi^+} + \varepsilon_{\phi\psi^-}] = \left\{ \frac{d_{\phi\psi^+} + d_{\phi\psi^-}}{2d_0} - 1 \right\}$$

$$= \{ \varepsilon_{11} \cos^2 \phi + \varepsilon_{12} \sin 2\phi + \varepsilon_{22} \sin^2 \phi - \varepsilon_{33} \} \sin^2 \psi + \varepsilon_{33} \quad (3.5a)$$

$$a_2 = \frac{1}{2} [\varepsilon_{\phi\psi^+} - \varepsilon_{\phi\psi^-}] = \left\{ \frac{d_{\phi\psi^+} - d_{\phi\psi^-}}{2d_0} \right\}$$

$$= \{ \varepsilon_{11} \cos \phi + \varepsilon_{23} \sin \phi \} \sin |2\psi| \quad (3.5b)$$

where a_1 and a_2 are defined parameters, $\psi_- = (-1)\psi_+$ and $\sin 2\psi^+ - \sin 2\psi^- = 2 \sin |2\psi|$.

Equation 3.5a shows a linear relation between a_1 and $\sin^2 \psi$. From the equation, slope and the intercept ($\psi = 0$) point can be derived,

$$m_{a_1} = \varepsilon_{11} \cos^2 \phi + \varepsilon_{12} \sin 2\phi + \varepsilon_{22} \sin^2 \phi - \varepsilon_{33} \quad (3.6a)$$

$$I_{a_1} = \varepsilon_{33} \quad (3.6b)$$

Similar to relationship between a_1 and $\sin^2 \psi$, there is a linear relation between a_2 and $\sin|2\psi|$. In this case the intercept ($\psi = 0$) is at point zero obviously, the slope is,

$$m_{a_2} = \varepsilon_{13} \cos \phi + \varepsilon_{23} \sin \phi \quad (3.7)$$

As a result, if $d_{\phi\psi}$ data is obtained over a range $\pm\psi$ at three ϕ tilts ($0^\circ, 45^\circ, 90^\circ$), and a_1 vs. $\sin^2 \psi$ and a_2 vs. $\sin|2\psi|$ are plotted for all ψ , the quantities $\varepsilon_{11} - \varepsilon_{33}$, $\varepsilon_{22} - \varepsilon_{33}$ and $\frac{1}{2}(\varepsilon_{11} + 2\varepsilon_{12} + \varepsilon_{22} - 2\varepsilon_{33})$ can be obtained from equation 3.7 for the corresponding tilts of ϕ . From the equation 3.6a it can be derived that the intercept of a_1 vs. $\sin^2 \psi$ gives ε_{33} for all the values of ψ . Similarly, using the slope of a_2 vs. $\sin|2\psi|$, the quantities ε_{13} , ε_{23} can be obtained in such a way that for $\phi=0^\circ$, equation 3.7 yields ε_{23} , and for $\phi=90^\circ$ it yields ε_{13} .

3.3.1.2. Linear $d_{\phi\psi}$ vs. $\sin^2 \psi$ Behavior (No ψ -Splitting)

Procedure for $d_{\phi\psi}$ vs. $\sin^2 \psi$ plot (Figure 3.2a) is also similar to the procedure of ψ -splitting except less data points are required. The strain tensor in the \underline{S}_i coordinate system is given by

$$\varepsilon_{ij} = \begin{vmatrix} \varepsilon_{11} & \varepsilon_{12} & 0 \\ 0 & \varepsilon_{22} & 0 \\ 0 & 0 & \varepsilon_{33} \end{vmatrix}$$

and $d_{\phi\psi}$ vs. $\sin^2 \psi$ data is required at positive (or negative) ψ values only. For this case equation 3.4 takes the form

$$\frac{d_{\phi\psi} - d_0}{d_0} = \{ \varepsilon_{11} \cos^2 \phi + \varepsilon_{12} \sin 2\phi + \varepsilon_{22} \sin^2 \phi - \varepsilon_{33} \} \sin^2 \psi + \varepsilon_{33} \quad (3.8)$$

the terms in the curl bracket of equation 3.8 is the same as right hand side of equation 3.7. Similar procedure can be followed to find values of the strain terms in the equation 3.8.

Stress Calculation

Calculation of the stresses using the strain values obtained from diffraction data is rather straight forward. The stress values of the sample coordinate system (\underline{S}_i) can be calculated using general form of Hooke's law [16,17]

$$\sigma_{ij} = C_{ijkl} \varepsilon_{kl} \quad (3.9)$$

where C_{ijkl} is fourth-order stiffness tensor and in sample coordinate system. The stresses in any other coordinate system can be determined using tensor transformation rule [16,17]:

$$\sigma'_{mn} = a_{mi} a_{nj} \sigma_{ij} \quad (3.10)$$

where a_{mi} and a_{nj} are the direction cosines.

The procedure is the basis for stress calculation of various types of diffraction techniques.

These equations will take different forms depending on the material properties of the sample and the stress state of resultant body shape.

The general case for an anisotropic material under stress

$$\sigma_{ij} = \begin{vmatrix} \sigma_{11} & \sigma_{12} & \sigma_{13} \\ 0 & \sigma_{22} & \sigma_{23} \\ 0 & 0 & \sigma_{33} \end{vmatrix} \quad (3.11)$$

Using the inverse of equation 3.9, the strains of the sample coordinate system can be expressed in terms of stresses:

$$\varepsilon_{ij} = S_{ijkl} \sigma_{kl} \quad (3.12)$$

where S_{ijkl} is the elastic compliance tensor[16].

When equation 3.12 substituted into equation 3.4, the relation between the stresses and the measured data is obtained. It is important to note that the elastic compliances are also referred to the sample coordinate system, therefore it must be obtained from the elastic constants referred to the unit cell axes (Figure 3.3), by again tensor transformation rule that was used previously.

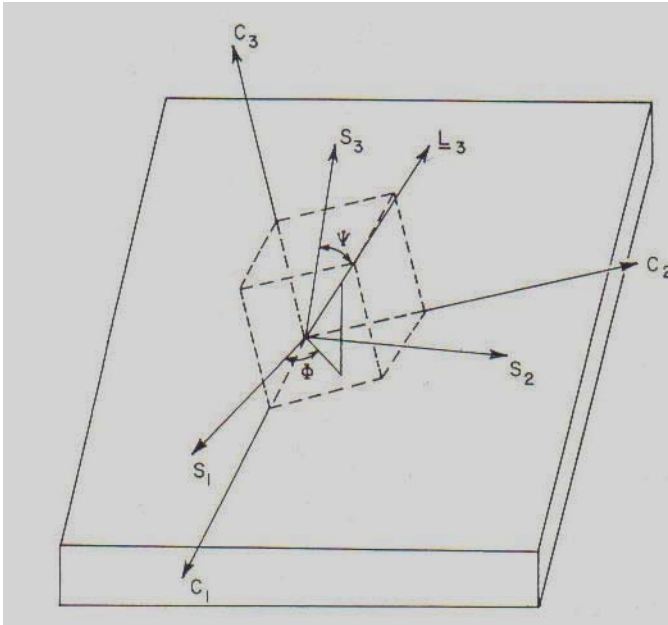


Figure 3.3. Crystal axes and their orientation with respect to laboratory and sample axes [6].

For instance,

$$\varepsilon_{11} = a_{1m} a_{1n} a_{k0} a_{lp} S_{mnop} \sigma_{kl} \quad (3.13)$$

where a_{k0} and a_{lp} are the direction cosines and S_{mnop} is the elastic compliance tensor defined in the crystal axes.

The next step is to link measured d values to the stresses in the sample coordinate system.

Equation 3.13 can be substituted into equation 3.4 to get the general equation.

For an isotropic material,

$$\varepsilon_{ij} = \frac{1+\nu}{E} \sigma_{ij} - \delta_{ij} \frac{\nu}{E} \sigma_{kk} \quad (3.14)$$

is the associated strain relation [16]. If the equation 3.8 is substituted into equation 3.4:

$$\begin{aligned}
\frac{d_{\phi\psi} - d_0}{d_0} &= \frac{1+\nu}{E} \left\{ \sigma_{11} \cos^2 \phi + \sigma_{12} \sin 2\phi + \sigma_{22} \sin^2 \phi - \sigma_{33} \right\} \sin^2 \psi \\
&+ \frac{1+\nu}{E} \sigma_{33} - \frac{\nu}{E} tr(\sigma) \\
&+ \frac{1+\nu}{E} \left\{ \sigma_{13} \cos \phi + \sigma_{23} \sin \phi \right\} \sin 2\psi
\end{aligned} \tag{3.15}$$

From the equation 3.15, it is clear that the stress tensor will be expected to be in one of the following forms:

$$\begin{pmatrix} \sigma_{11} & 0 & 0 \\ 0 & \sigma_{22} & 0 \\ 0 & 0 & 0 \end{pmatrix}, \begin{pmatrix} \sigma_{11} & \sigma_{12} & 0 \\ 0 & \sigma_{22} & 0 \\ 0 & 0 & 0 \end{pmatrix}, \begin{pmatrix} \sigma_{11} & 0 & 0 \\ 0 & \sigma_{22} & 0 \\ 0 & 0 & \sigma_{33} \end{pmatrix}, \begin{pmatrix} \sigma_{11} & \sigma_{12} & 0 \\ 0 & \sigma_{22} & 0 \\ 0 & 0 & \sigma_{33} \end{pmatrix} \tag{3.16a, b, c, d}$$

3.4. Biaxial Stress Analysis

3.4.1. The “ $\sin^2 \psi$ ” Method

If the sample has a biaxial stress state, then the equation 3.15 takes the form

$$\frac{d_{\phi\psi} - d_0}{d_0} = \frac{1+\nu}{E} \sigma_{\phi} \sin^2 \psi - \frac{\nu}{E} (\sigma_{11} + \sigma_{22}) \tag{3.17}$$

where σ_{ϕ} is the stress component along the \underline{S}_{ϕ} direction (Figure 3.3). It is given by

$$\sigma_{\phi} = \sigma_{11} \cos^2 \phi + \sigma_{22} \sin^2 \phi \tag{3.18a}$$

$$\sigma_{\phi} = \sigma_{11} \cos^2 \phi + \sigma_{12} \sin 2\phi + \sigma_{22} \sin^2 \phi \tag{3.18b}$$

for the stress tensors given in equations (3.16a,b) respectively.

Equation 3.17 is the common x-ray residual stress equation. It predicts a linear behavior of $d_{\phi\psi}$ vs. $\sin^2 \psi$. In this case, experimental data is used to obtain the least-squares line. Then, the stress in σ_{ϕ} direction is the slope of the least-squares line supposing material constants E, ν and unstressed d -spacing (d_0) are known. This method is known as $\sin^2 \psi$, because it utilizes multiple ψ values. There are various ways to evaluate d_0 [5,6]. The lattice spacing measured at $\psi = 0$ is substituted for d_0 in this experiment. This substitution is based on the fact that, most of the materials, elastic strains do not introduce more than 0.1% difference between the true d_0 and d at any ψ . The error of such usage is less than 0.1%, because d_0 is a multiplier to the slope. Therefore this much error is omitted compared to other error sources that will be discussed later.

3.4.2. The Two-Tilt Method

This method is usually used for rapid testing. The method assumes a linear variation of d with $\sin^2 \psi$. Hence only two tilts will be enough to define the line ($\psi, \psi=0$).

For this method a simplified version of the equation 3.17 can be written as:

$$\frac{\Delta d}{d} = \frac{1+\nu}{E} \sigma_{\phi} \sin^2 \psi - \frac{\nu}{E} (\sigma_{11} + \sigma_{22}) \quad (3.19)$$

The term on left side of equation 3.19 can be written in terms of the shift in 2θ of the diffracted intensity between these two tilts ($\psi, \psi=0$).

If Bragg's law is differentiated:

$$\frac{\Delta d}{d} = -\frac{\cot \theta (\Delta 2\theta)}{2} \quad (3.20)$$

From equations 3.19 & 3.20,

$$\sigma_{\phi} = \left(\frac{E \cot \theta}{2(1+\nu) \sin^2 \psi} \right) \Delta 2\theta \quad (3.21)$$

where $\Delta 2\theta$ is the peak-shift. The term in the parenthesis at the right side of the equation 3.21 is the stress constant.

$$K = \frac{E \cot \theta}{2(1+\nu) \sin^2 \psi} \quad (3.22)$$

This method is practical for small values of $\Delta 2\theta$. Equation 3.22 is not valid for large values of $\Delta 2\theta$. For the large values of $\Delta 2\theta$, equation 3.19 will be still valid [5,6].

3.5. Triaxial Stress Analysis

The two methods of biaxial stress analysis which was discussed in the previous section assume that the stress components in the direction of the surface normal are negligible. However, that assumption may not be true for some cases. ψ -splitting shows the existence of those strain components that were neglected in biaxial stress analysis.

In fact, existence of the strain components in the direction of normal to the surface of the sample indicates the presence of the stress components in this direction.

Analysis of stresses for ψ -split case of the d vs. $\sin^2 \psi$ behavior is similar to that of strains. In this case the terms (a_1, a_2) will be expressed in terms of stresses instead of strains:

$$\begin{aligned}
a_1 &= \left\{ \frac{d_{\phi\psi^+} + d_{\phi\psi^-}}{2d_0} - 1 \right\} \\
&= \frac{1+\nu}{E} \{ \sigma_{11} \cos^2 \phi + \sigma_{12} \sin 2\phi + \sigma_{22} \sin^2 \phi - \sigma_{33} \} \sin^2 \psi \\
&\quad + \frac{1+\nu}{E} \sigma_{33} - \frac{\nu}{E} (\sigma_{11} + \sigma_{22} + \sigma_{33})
\end{aligned} \tag{3.23}$$

$$a_2 = \left\{ \frac{d_{\phi\psi^+} - d_{\phi\psi^-}}{2d_0} \right\} = \frac{1+\nu}{E} \{ \sigma_{13} \cos \phi + \sigma_{23} \sin \phi \} \sin |2\psi| \tag{3.24}$$

Hence, the stress components in equation 3.23 can be obtained from the slope and intercept of a_1 vs. $\sin^2 \psi$ for $\phi = 0^\circ$, 45° , and 90° . On the other hand the stress components of the equation 3.24 will be obtained from the a_2 vs. $\sin |2\psi|$ for the same values of ϕ except 45° . Once the stress tensor in the sample coordinate system is obtained, it can be transformed to the any coordinate system via tensor transformation rule that was discussed earlier.

If the stress components of the equation 3.24 are zero, then it suggests that d vs. $\sin^2 \psi$ plot is linear. Then equation 3.15 reduces to

$$\begin{aligned}
(\epsilon'_{33})_{\phi\psi} &= \frac{d_{\phi\psi} - d_0}{d_0} = \frac{1+\nu}{E} \{ \sigma_{11} \cos^2 \phi + \sigma_{12} \sin 2\phi + \sigma_{22} \sin^2 \phi - \sigma_{33} \} \sin^2 \psi \\
&\quad + \frac{1+\nu}{E} \sigma_{33} - \frac{\nu}{E} tr(\sigma)
\end{aligned} \tag{3.25}$$

If the equations 3.17 and 3.25 are compared, the stress σ_ϕ determined by the method of biaxial stress analysis will contain an error of magnitude σ_{33} . For the sake of eliminating this error, the following methodology can be utilized:

If the data obtained for the two tilts, $\phi = \phi_A$, $\phi = \phi_A + 90^\circ$, then it is possible to find the slopes of the $(\varepsilon'_{33})_{\phi\psi}$ vs. $\sin^2 \psi$ graphs,

$$\begin{aligned} m_{\phi_A} &= \frac{1+\nu}{E} \{ \sigma_{11} \cos^2 \phi_A + \sigma_{12} \sin 2\phi_A + \sigma_{22} \sin^2 \phi_A - \sigma_{33} \} \\ &= \frac{1+\nu}{E} (\sigma_{\phi_A} - \sigma_{33}) \end{aligned} \quad (3.26a)$$

$$\begin{aligned} m_{\phi_A+90^\circ} &= \frac{1+\nu}{E} \{ \sigma_{11} \cos^2(\phi_A + 90) + \sigma_{12} \sin 2(\phi_A + 90) + \sigma_{22} \sin^2(\phi_A + 90) - \sigma_{33} \} \\ &= \frac{1+\nu}{E} (\sigma_{\phi_A+90} - \sigma_{33}) \end{aligned} \quad (3.26b)$$

The sum of these two slopes is

$$m_{\phi_A} + m_{\phi_A+90^\circ} = \frac{1+\nu}{E} (\sigma_{11} + \sigma_{22} - 2\sigma_{33}) \quad (3.27)$$

The intercept is

$$I = \left(\frac{1+\nu}{E} \right) \sigma_{33} - \frac{\nu}{E} \text{tr}(\sigma) \quad (3.28)$$

It is important to note that the intercept of $(\varepsilon'_{33})_{\phi\psi}$ vs. $\sin^2 \psi$ does not depend on the angle ϕ [5,6].

3.6. Determination of Unstressed d-spacing

As it was mentioned in the previous sections, there are various ways to determine the unstressed lattice spacing d_0 . Based on the biaxial assumption, the lattice spacing measured at $\psi = 0$ is substituted for d_0 due to the fact that this assumption introduces a negligible amount of error. Another method uses the data obtained during stress

measurement itself. If the stress state is biaxial, this method can be used to determine exact d_0 from the d vs. $\sin^2 \psi$ graph. For $\phi = 0$, equation 3.17 takes the form

$$\frac{d_{\phi\psi} - d_0}{d_0} = \frac{1+\nu}{E} \sigma_{11} \sin^2 \psi - \frac{\nu}{E} (\sigma_{11} + \sigma_{22}) \quad (3.29)$$

Suppose, if for $\psi = \psi'$, $d_{0\psi'} = d_0$, then the equation 3.22 will take the form

$$\sin^2 \psi' = \frac{\nu}{1+\nu} \left(1 + \frac{\sigma_{22}}{\sigma_{11}} \right) = \frac{\nu}{1+\nu} \left(1 + \frac{m_2}{m_1} \right) \quad (3.30)$$

where m_1 and m_2 are the slopes of the plot for $\phi = 0^\circ, 90^\circ$ respectively. Once the equation 3.30 is solved for $\sin^2 \psi'$, then d_0 can be determined from d vs. $\sin^2 \psi$ for $\phi = 0$ [6].

The triaxial case has the procedure which is similar to that of the biaxial case.

For $\phi = 0$, and if, $\psi = \psi'$, $d_{0\psi'} = d_0$ then equation 3.25 will take the form

$$\sin^2 \psi' = \frac{-(1+\nu)\sigma_{33} + \nu \text{tr}(\sigma)}{(1+\nu)(\sigma_{11} - \sigma_{33})} \quad (3.31)$$

Equation 3.31 can further be simplified by

$$\sin^2 \psi' = \frac{\nu}{(1+\nu)} \left\{ 1 + \frac{\sigma_{22} - \sigma_{33}}{\sigma_{11} - \sigma_{33}} \right\} = \frac{\nu}{(1+\nu)} \left(1 + \frac{m_2}{m_1} \right) \quad (3.32)$$

where terms m_1 and m_2 can be obtained using the procedure of biaxial method explained earlier. The difference of this case comes from the assumption made to obtain the simplified equation. Due to the fact that, it may introduce large amount of errors, this method should not be used for the higher values of σ_{33} .

IV. EXPERIMENTAL TECHNIQUES

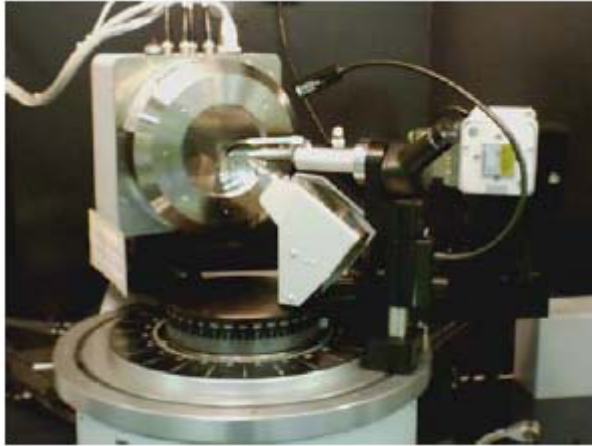


Figure 4.1. Bruker-AXS GADDS 2D powder and single-crystal X-Ray diffractometer, Department of Chemistry, Texas A&M University.

For measurement of diffraction events from regular and irregularly shaped samples. The instrument employs;

- the H-star multi-wire two-dimensional area detector (1024 x 1024 pixel size)
- a Cu X-ray tube.

A small monochromatic X-ray beam is used to probe micro and irregular areas.

Common applications of the diffractometer (Figure 4.1) can be summarized as follows;

- Powder and polymer diffraction
- Single-crystal structure determination
- Pole figure measurements
- Residual stress measurements (normal and shear)
- Determination of crystallinity of polycrystalline materials
- Preferred orientation of samples [18].

4.1. Material Under Investigation

The material investigated in this paper is SS316.

Material properties of SS316 [19].

$$E= 193 \text{ Gpa} \quad \nu= 0.29$$

Table 4.1 and Table 4.2 give chemical composition and physical properties of SS316.

Table 4.1. Chemical composition of SS316 [4].

Chemistry Data	
Carbon	0.08 max
Chromium	16 - 18
Iron	Balance
Manganese	2 max
Molybdenum	2 - 3
Nickel	10 - 14
Phosphorus	0.045 max
Silicon	1 max
Sulphur	0.03 max

Table 4.2. Physical properties of SS316 [4].

Physical Data	
Density	0.288 (lb / cu. In.)
Specific Gravity	7.95
Specific Heat [32-212 °F]	0.12 Btu/lb/Deg °F
Electrical Resistivity (at 68 Deg °F)	445 microhm-cm
Melting Point	2550 Deg °F
Modulus of Elasticity	193 GPa

4.2. Sample Preparation

For the sake of being consistent, each sample was prepared in the same way. This way amount of error due to sample preparation will be reduced to a minimum amount. It is also important to note that, it is unavoidable to introduce new stresses to the samples during sample preparation. However, amount that is introduced during the preparation reduced to minimum by taking necessary precautions. For instance, first a diamond saw used to obtain small samples, and then these small samples were cut using a precision cut to get smaller samples. Hence, instead of obtaining samples at one step, several steps were taken to reduce the amount of error due to preparation step. Also, each sample was cut along the wavy lines if it was possible.

Calculation of residual stress of some samples together with the graphs of the experimental data will be given as examples in the next section, and than residual stress values of the rest of the samples will be given as tabulated.

V. RESULTS AND DISCUSSIONS

In this section, typical x-ray diffraction data will be shown. Then the way this data is used in calculations will be explained. Afterwards, residual stress calculation of some samples will be given. However, the calculations of each sample will not be included here. Residual stress values for the samples will be tabulated. Table 5.1 gives the abbreviations of the samples used in the experiment.

Table 5.1. The abbreviations of the samples.

Abbreviation	Process
B1	2_150_4CPI STAMPED
B2	2_150_8CPI STAMPED
B3	6_150_4CPI STAMPED
B4	6_150_8CPI STAMPED
B5	8_300_8CPI ROLLED
B6	8_300_8CPI SEGMENT
B7	UNPROCESSED
B8	8_300_4CPI STAMPED

5.1. Residual Stress Calculations

Considering the thickness of the material, biaxial stress analysis was carried out.

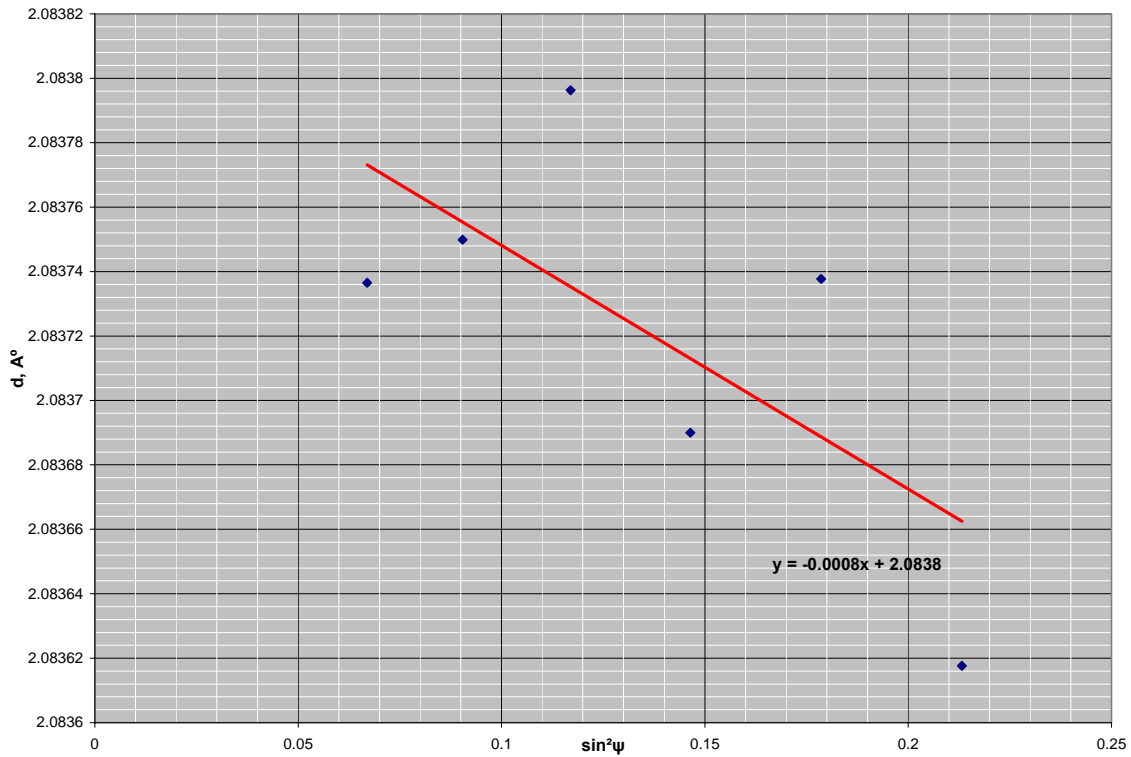


Figure 5.1. A linear graph of d vs. $\sin^2 \psi$ fitted to diffraction data with a negative slope.

Figure 5.1 shows a least square line fitted to data obtained from the x-ray diffraction.

Figure 5.1 exhibits a regular d vs. $\sin^2 \psi$ behavior, which suggests the use of the equation 3.17.

$$\frac{d_{\phi\psi} - d_0}{d_0} = \frac{1+\nu}{E} \sigma_{\phi} \sin^2 \psi - \frac{\nu}{E} (\sigma_{11} + \sigma_{22})$$

This equation can be modified as

$$d_{\phi\psi} = d_0 \frac{1+\nu}{E} \sigma_{\phi} \sin^2 \psi - d_0 \frac{\nu}{E} (\sigma_{11} + \sigma_{22}) + d_0 \quad (5.1)$$

multiplier of the $\sin^2 \psi$ term is the slope of the d vs. $\sin^2 \psi$ graph. Equation 5.1 can be rearranged for the slope m ,

$$m = d_0 \frac{1+\nu}{E} \sigma_{\phi} \quad (5.2)$$

Equation 5.2 can be further modified to give the stress,

$$\sigma_{\phi} = \frac{m}{d_0} \left(\frac{E}{1+\nu} \right) \quad (5.3)$$

The equation 5.3 is a very simple equation,

$$\sigma_{\phi=30^\circ} = \frac{-0.0008}{2.18516} \left(\frac{193}{1+0.29} \right) 10^9 Pa$$

$$\sigma_{\phi=30^\circ} = -54.774 MPa$$

The residual stress calculation for Figure 5.2 is similar to that of Figure 5.1. It follows, using equation 5.3

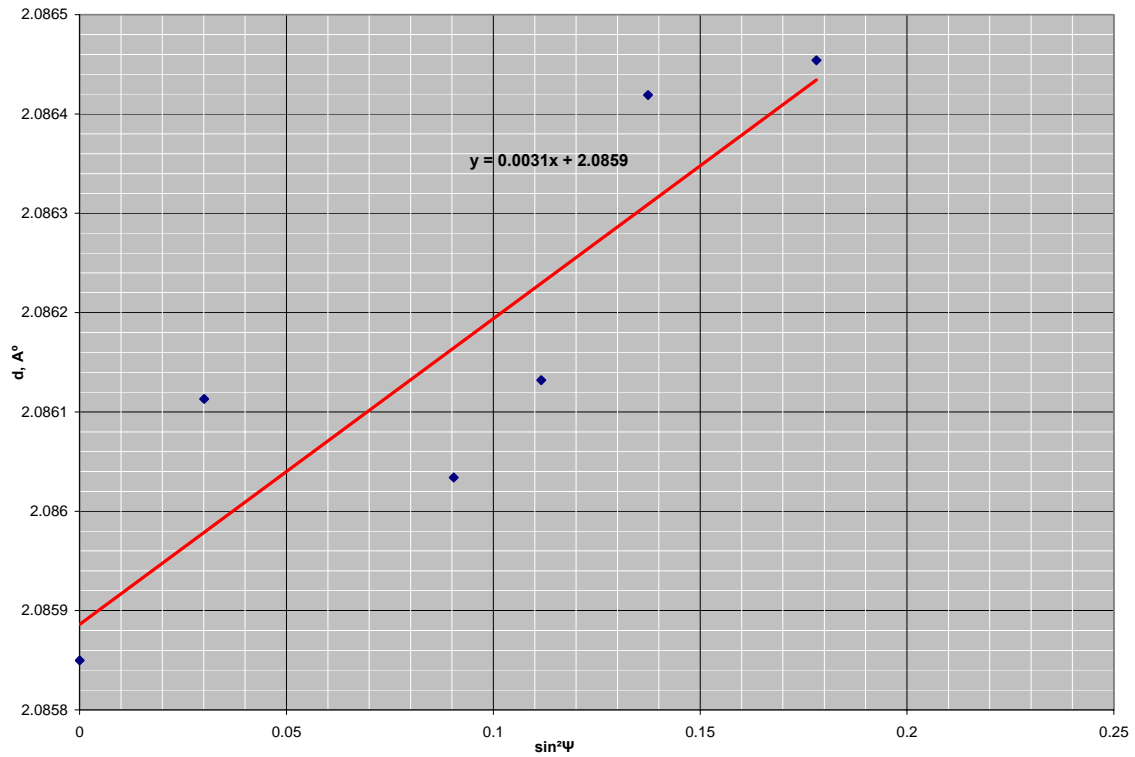


Figure 5.2. A linear graph of d vs. $\sin^2 \psi$ fitted to diffraction data with a positive slope.

$$\sigma_{\phi=30^\circ} = \frac{m}{d_0} \left(\frac{E}{1+\nu} \right)$$

$$\sigma_{\phi=30^\circ} = \frac{0.0031}{2.18516} \left(\frac{193}{1+0.29} \right) 10^9$$

The stress component along the \underline{S}_ϕ direction will be

$$\sigma_{\phi=30^\circ} = 212.249 \text{ MPa}$$

Table 5.2. X-ray diffraction data for **B6**, $\Psi=30$ $\phi=90$.

Legend Angle 2-Theta °	d value Angstrom	Intensity %	h	k	l
2Th = 43.449 °	d = 2.08102	I = 53.6 %	2.08102	11.2	53.6
2Th = 50.735 °	d = 1.79793	I = 77.7 %	1.79793	16.3	77.7
2Th = 72.569 °	d = 1.30160	I = 22.7 %	1.30160	4.75	22.7
2Th = 74.573 °	d = 1.27150	I = 71.6 %	1.27150	15.0	71.6
2Th = 76.375 °	d = 1.24593	I = 35.8 %	1.24593	7.49	35.8
2Th = 77.659 °	d = 1.22851	I = 23.8 %	1.22851	4.97	23.8
2Th = 86.461 °	d = 1.12460	I = 30.7 %	1.12460	6.42	30.7
2Th = 90.652 °	d = 1.08320	I = 100.0 %	1.08320	20.9	100.0
2Th = 95.697 °	d = 1.03899	I = 68.3 %	1.03899	14.3	68.3
2Th = 67.108 °	d = 1.39360	I = 22.3 %	1.39360	4.66	22.3
2Th = 71.649 °	d = 1.31603	I = 23.1 %	1.31603	4.83	23.1
2Th = 69.691 °	d = 1.34814	I = 21.3 %	1.34814	4.46	21.3

Table 5.2 shows part of typical x-ray diffraction results for B6. The data in red indicates the angle and the d-spacing which is used in calculations, because the relative intensity has the maximum intensity at this value. Next, some portion of sample B2 data for the angles $\psi = 30^\circ$, $\phi = 90^\circ$ together with the associated graph is given in Table 5.3 and Figure 5.3 respectively.

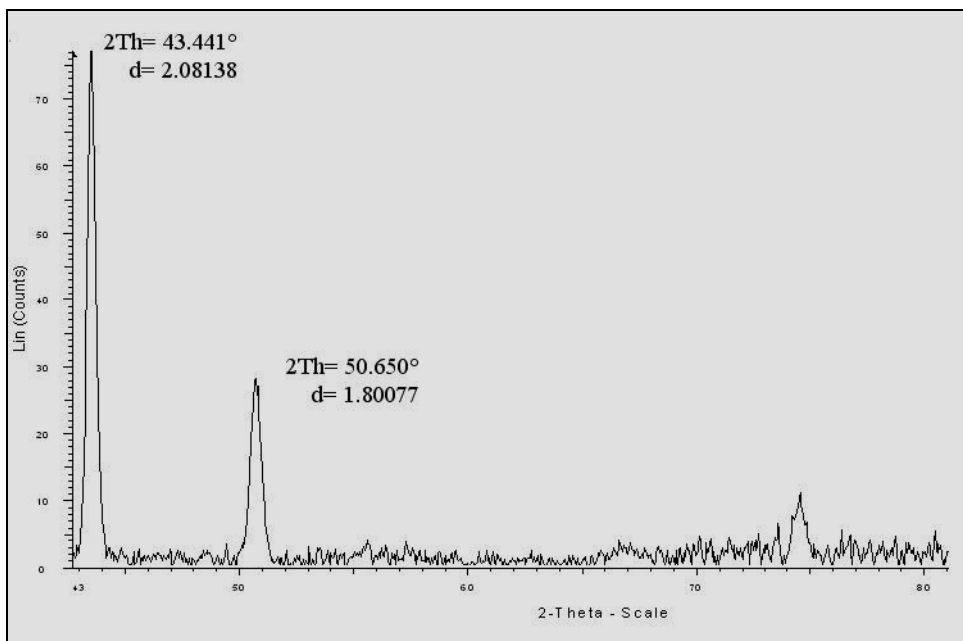


Figure 5.3. Two peak values of scattering angle θ are given together with the corresponding d-spacing values for B4.

Table 5.3. Part of X-ray diffraction data for B2.

Angle	d	Intensity	h	k	l
2Th = 43.441 °,	d = 2.08138,	I = 100.0 %	2.08138	77.5	100.0
2Th = 50.650 °,	d = 1.80077,	I = 36.9 %	1.80077	28.6	36.9
2Th = 68.325 °,	d = 1.37172,	I = 3.9 %	1.37172	3.06	3.9
2Th = 73.595 °,	d = 1.28597,	I = 9.6 %	1.28597	7.46	9.6
2Th = 82.308 °,	d = 1.17048,	I = 5.3 %	1.17048	4.14	5.3
2Th = 88.911 °,	d = 1.09984,	I = 7.3 %	1.09984	5.62	7.3

Next, the graphs of B4 at different ϕ° and ψ° values will be shown (Figures 5.4a, b, c). The values in red show the maximum relative intensity and the corresponding values of the diffraction angle along with the d-spacing value. h, k, l values may be used to determine the set of parallel planes that cause the diffraction.

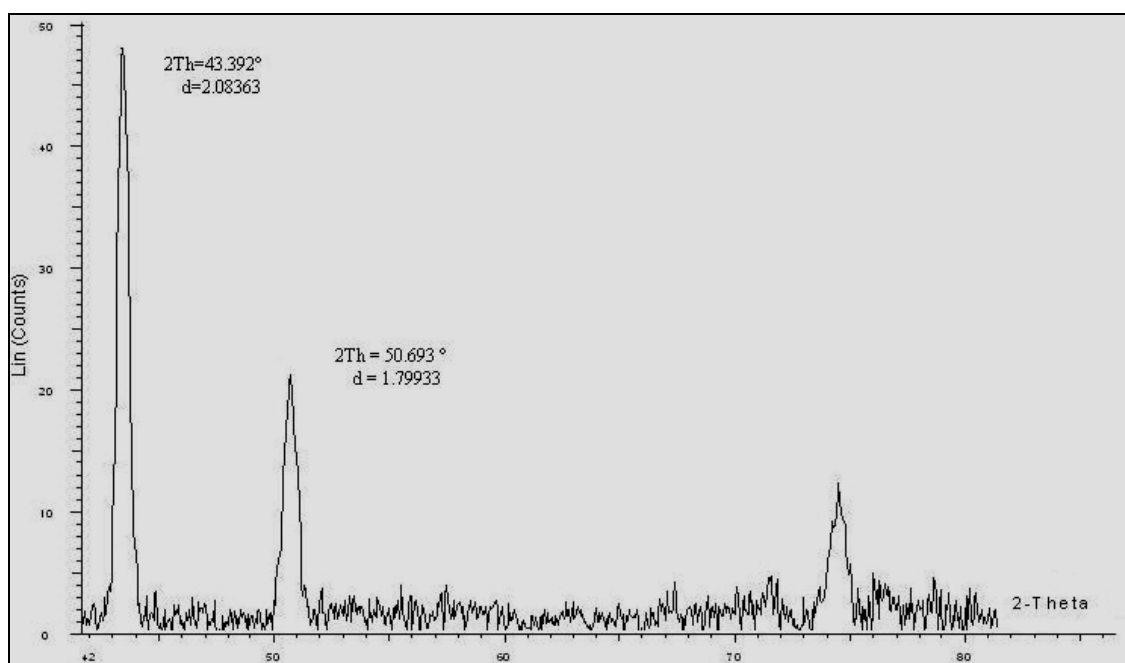


Figure 5.4a. Peak values for $\psi = 15^\circ$ and $\phi = 0^\circ$ of B4.

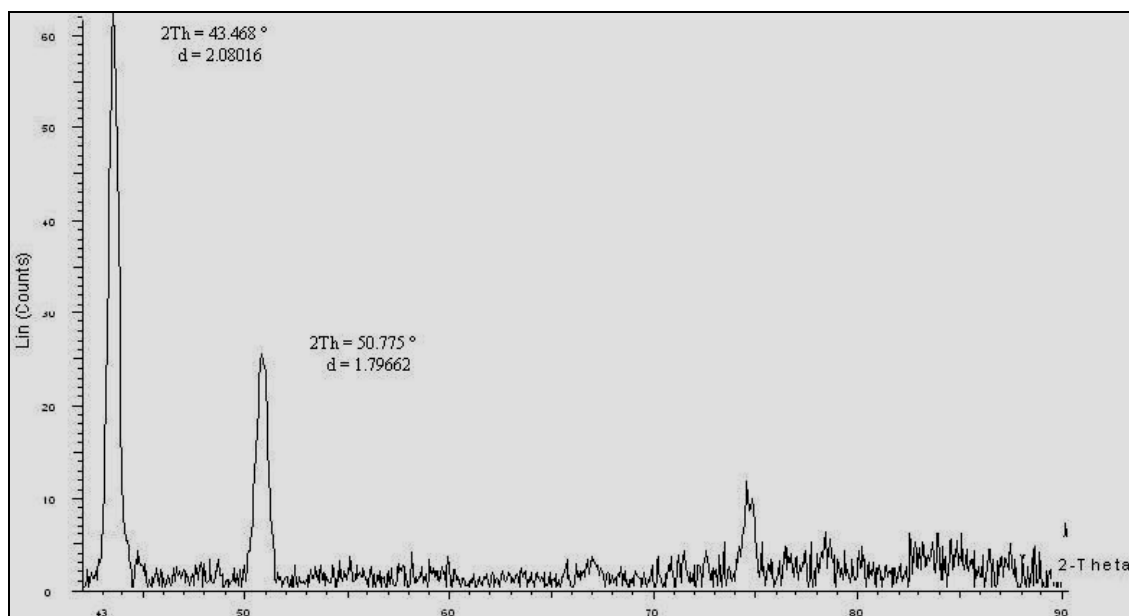


Figure 5.4b. Peak values for $\psi = 15^\circ$ and $\phi = 45^\circ$ of B4.

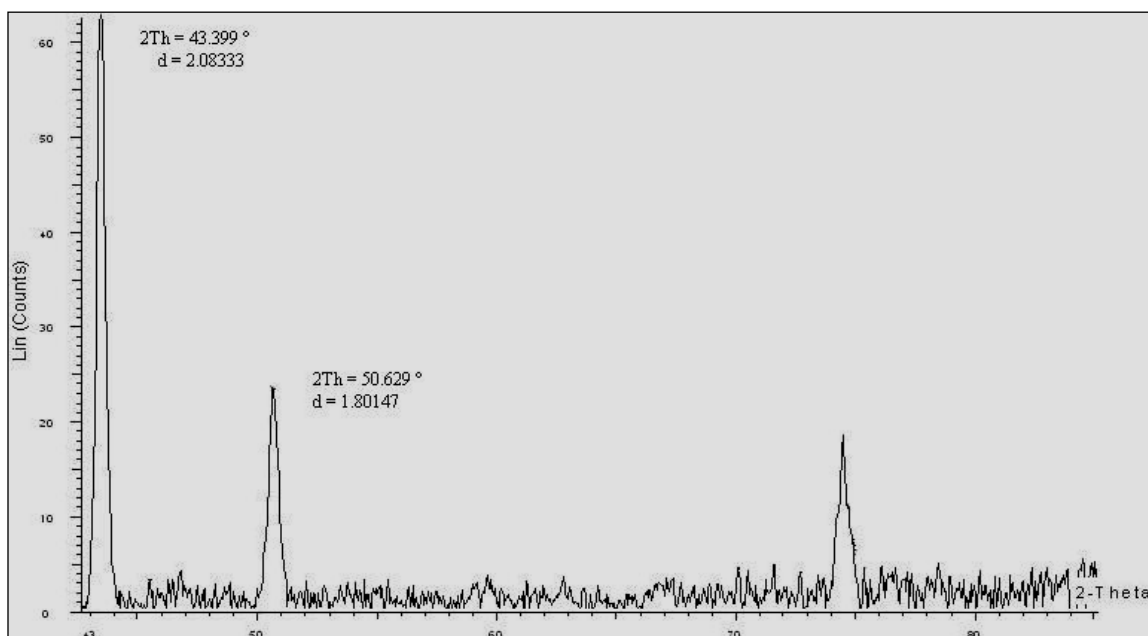


Figure 5.4c. Peak values at $\psi = 30^\circ$ and $\phi = 0^\circ$ of B4.

Table 5.4. Comparison of two peak data at three different angles of B4.

Sample: B4	$2\theta^\circ$	d-spacing	h	k	L
$\psi = 15^\circ, \phi = 0^\circ$	43.392 °	2.08363	2.08363	48.1	100.0
$\psi = 15^\circ, \phi = 45^\circ$	43.468 °	2.08016	2.08016	62.7	100.0
$\psi = 30^\circ, \phi = 0^\circ$	43.399 °	2.08333	2.08333	63.4	100.0
$\psi = 15^\circ, \phi = 0^\circ$	50.693 °	1.79933	1.79933	21.4	44.4
$\psi = 15^\circ, \phi = 45^\circ$	50.775 °	1.79662	1.79662	25.5	40.7
$\psi = 30^\circ, \phi = 0^\circ$	50.629 °	1.80147	1.80147	23.3	36.8

Table 5.4 compares the two peak values of B4 at different angles.

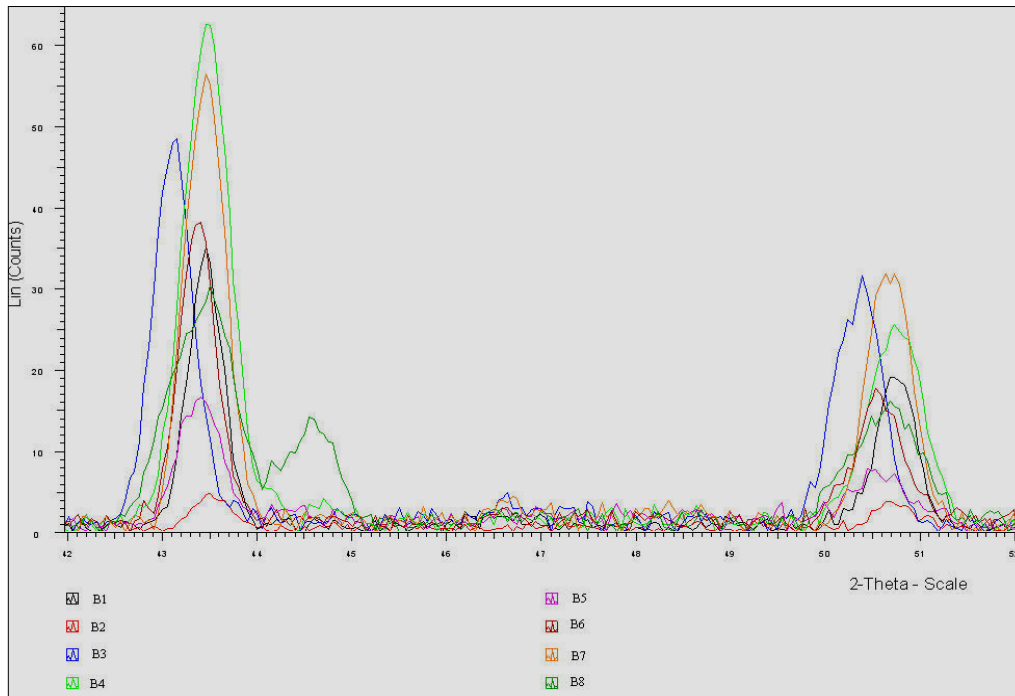


Figure 5.5a. Peaks of all 8 samples are shown for $\Psi=15^\circ$, $\phi=45^\circ$

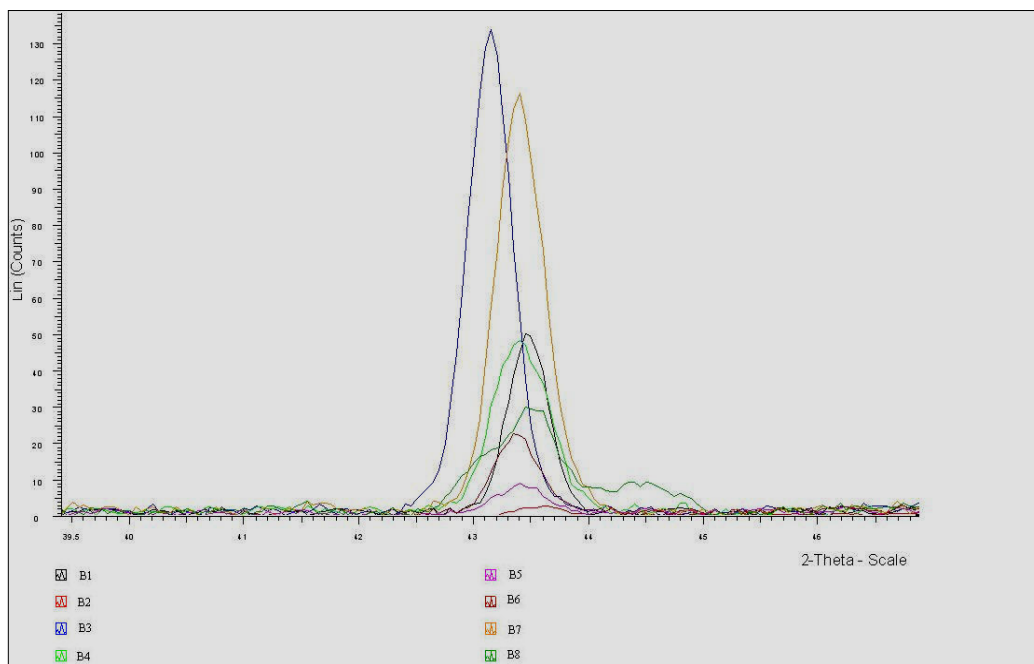


Figure 5.5b. Peaks for all 8 samples are shown for $\Psi=15^\circ$, $\phi=00^\circ$

Figures 5.5a, b show the peaks of the samples. Residual stress values of all 8 samples are given below in Table 5.5.

Table 5.5. Residual stress values of the samples.

Residual Stress Values ($\sigma_{\phi=30^\circ}$) in MPa for $\phi = 30^\circ$							
B1	B2	B3	B4	B5	B6	B7	B8
-54.274	95.327	170.872	200.227	190.872	-160.254	___	212.249

For the 7 given samples, the assumption of biaxial method made the calculations straightforward. Using the associated equations for the method the residual stress values of the samples were determined. For the second set of samples, however the method was not applicable due to existence of texture in the grains. Figure 5.6 shows the oscillatory behavior of the curve for the data. Such behavior suggests that the material under investigation is textured.

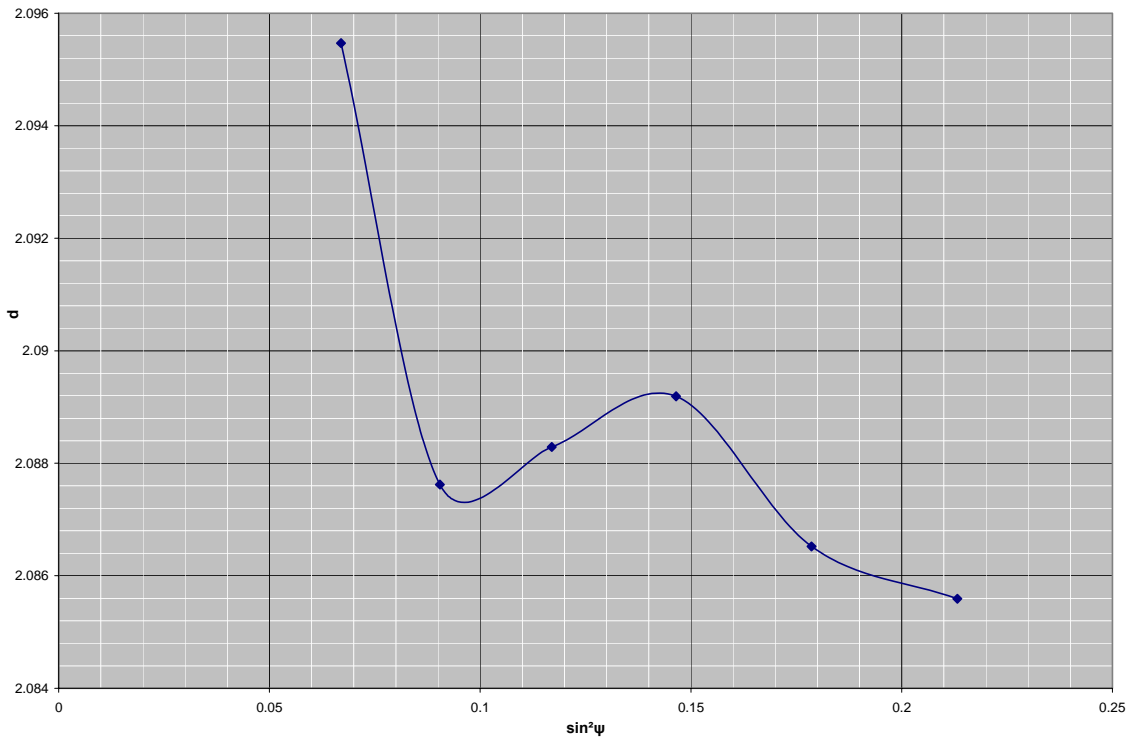


Figure 5.6. The curve exhibits oscillatory behavior.

If the material under investigation is textured, then the material values given cannot be used directly. For the textured materials, the x-ray elastic constants are used instead of E and ν . These constants can be obtained from the literature for a given material and reflection combination. It is also possible to obtain these values experimentally. In this method of experimentally determining elastic constants the specimen is stressed on a diffractometer with a known magnitude of load. Then using available equipment which is usually microprocessor controlled device that is capable of determining elastic constants, those values can be obtained. Uniaxial tensile loading or

four-point bending is usually employed. Table 5.6 shows the x-ray elastic constants for some materials for the given radiations.

Table 5.6 X-ray elastic constants of some materials [6].

MATERIAL	Radiation	$(1+\nu)/E$ $\times 10^{-8}$	Hkl
Aluminum	Co	14.09	420
ARMCO Fe	Cr	2.41	211
1045	Cr	3.50	211
1045	Co	4.99	310
0.73 %C Steel	Cr	4.38	211
0.39 %C Steel	Cr	3.88	220
Copper	Co	10.62	400
Nickel	Cu	4.36	420
304SS	Cr	4.95	220

VI. CONCLUSIONS

The X-ray diffraction (XRD) is one of the best developed methods available for residual stress determination. It is a non destructive technique. XRD technique uses the distance between crystallographic planes (d-spacing) as a strain gage. This method can only be applied to crystalline, polycrystalline and semi-crystalline materials. When the material is in tension, the d-spacing increases and when the material is in compression, the d-spacing decreases. Among the samples, B1 and B6 have negative values of residual stresses which means the state of residual stress exist in the both samples are compressive. On the other hand, for the rest of the samples it is tensile since they have positive values of residual stresses.

The presence of residual stresses in the material produces a shift in the x-ray diffraction peak angular position that is directly measured by the detector. In Figures 5.5a, b the shift in the peak positions can be observed for different samples. It is important to obtain a diffraction peak of suitable intensity. The peaks must be free of interference from neighboring peaks. So that the diffraction angle 2-theta can be measured experimentally and the d-spacing is then calculated using Bragg's law.

The most common problems in using X-ray diffraction technique arise due to the location of diffraction peak. For peak fitting purposes, the high precision is necessary which in turn requires accurate sample alignment and precise methods of diffraction peak location.

One of the major disadvantages with XRD is the limitation imposed on the test piece size and geometry. The geometry has to be such that an X-ray can both hit the measurement area and still be diffracted to the detector without hitting any obstructions. However, due to irregular geometry of some of the samples, it was not possible to get clear diffraction data.

The method is valid for isotropic and anisotropic materials. However it is necessary to have homogenous strain distribution within the material. Experimental data for the first set of samples indicated that $d_{\phi\psi}$ vs. $\sin^2 \psi$ behavior is linear. On the other hand, that was not the case for the second set of samples. The oscillatory behavior of the samples indicates the presence of inhomogeneous stress distribution. Analysis of this data with regular procedure would cause large errors. Analysis of the second set of samples may be part of future work.

6.1. Sources of Errors

In addition to the factors mentioned in the previous section, a number of factors can contribute to the introduction of error in the measurements. These parameters can be summarized as the following:

- Collection time.
- Number of Psi angles for $\sin^2 \psi$ technique.
- Peak location method.
- Surface curvature.
- Aperture size.
- Oscillation.

6.2. Future Work

- In addition to the biaxial method, the triaxial method can be used. The results of these two techniques can be compared.
- A better fitting program can be used to get peak values, so that the amount of error introduced during calculation can be reduced.
- Number of data points can be increased to get more accurate results.
- Surfaces of the samples can be cleaned using proper chemicals to eliminate any possible error due to surface.
- Samples can be run more than once, so that repeatability of the technique can be shown.
- Calculation of proportions of macro and micro stresses.
- X-ray residual stress determination of textured samples.

REFERENCES

1. Withers PJ, Bhadeshia HKDH, Overview: Residual Stress, Part 1—Measurement Techniques, *Materials Science and Technology* 2000; 17: 355.
<http://www.msm.cam.ac.uk/phase-trans/2001/mst4640a.pdf> (Accessed: 9.02.2004)
2. Physics & Industry, Residual Stress Theory, Definition of Residual Stress
http://www.physiqueindustrie.com/residual_stress.htm#Definition (Accessed: 9.12.2004)
3. Kandil FA, Lord JD, Fry AT, Grant PV, A Review of Residual Stress Measurement Methods-A Guide to Technique Selection, NPL Report MATC(A)04, 2001; 25-32.
4. Metal Suppliers Online, Properties of 316
<http://www.supplersonline.com/research/property/metals/1852.asp> (Accessed: 10.08.2004)
5. James M, Lu J, Roy G, *Handbook of Measurement of Residual Stress*: Englewood Cliffs, NJ: Prentice Hall; 1996.
6. Noyan IC, Cohen JB, *Residual Stress Measurement by Diffraction and Interpretation*, New York: Springer-Verlag; 1987.
7. Vrána M, Mikula P, Nový Z, Neutron Diffraction Measurements of Strain/Stress State Induced by a Weld Deposited Pass
<http://www.xray.cz/epdic/abstracts/166.htm> (Accessed: 10.02.2004)
8. Georgia State University, Department of Physics and Astronomy, HyperPhysics, Index, X-rays
<http://hyperphysics.phy-astr.gsu.edu/hbase/quantum/xtube.html> (Accessed: 10.02.2004)

9. Suryanarayana C, Norton MG, X Ray Diffraction A Practical Approach, New York: Plenum Press; 1998.
10. X-ray Mass Attenuation Coefficients, The Mass Attenuation Coefficient
<http://physics.nist.gov/PhysRefData/XrayMassCoef/chap2.html> (Accessed: 10.02.2004)
11. Giancoli DC, General Physics, Upper Saddle River, NJ: Prentice-Hall; 1984.
12. The Atomic Scattering Factor Files
http://www-cxro.lbl.gov/optical_constants/asf.html (Accessed: 10.01.2004)
13. X-ray Data Booklet, Section 1.7 Atomic Scattering Factors
http://xdb.lbl.gov/Section1/Sec_1-7.pdf (Accessed: 10.03.2004)
14. Reed-Hill RE, Abbaschian R, Physical Metallurgy Principles, Boston: PWS Publishing; 1991.
15. Cullity BD, Elements of X-Ray Diffraction, Reading, MA: Addison Wesley Publishing; 1978.
16. Slaughter W, The Linearized Theory of Elasticity, Boston: Birkhauser; 2002.
17. Reddy JN, Mechanics of Laminated Composite Plates, Boca Raton, FL: CRC Press; 1997.
18. X-ray Diffraction Laboratory, Bruker-AXS D8 Powder High Resolution Parallel Beam X-ray Diffractometer
<http://www.chem.tamu.edu/xray/pdf/brochure.pdf> (Accessed: 10.03.2004)
19. Engineering Fundamentals, Materials, Metal Alloys, Stainless Steels
<http://www.efunda.com> (Accessed: 10.06.2004)

VITA

Osman Anderoglu, son of Ahmet Muhtar and Elif Anderoglu and brother of Eyup, Hamza and Muhammed Emin, was born in Istanbul, Turkey in 1979. He graduated from Bogazici University, Department of Mechanical Engineering in May 2001. He enrolled in Texas A&M University to pursue a graduate degree in the fall 2002. He completed his research and received a Master of Science degree in mechanical engineering in December 2004. Following graduation, Osman will continue his studies at the University of Waterloo, Ontario, Canada. His permanent address is:

Cinar Mahallesi

10/1 Sokak, No:17

34560

Bagcilar, Istanbul, Turkey